

Jet power extracted from ADAFs and the application to Fermi BL Lacertae objects

Yongyun Chen(陈永云)^{*}¹, Qiusheng Gu(顾秋生)[†]², Junhui Fan(樊军辉)³, Xiaoling Yu(俞效龄)¹,

Nan Ding(丁楠)⁴, Xiaotong Guo(郭晓通)⁵, Dingrong Xiong(熊定荣)⁶

¹*College of Physics and Electronic Engineering, Qijiang Normal University, Qijiang 655011, P.R. China*

²*School of Astronomy and Space Science, Nanjing University, Nanjing 210093, P. R. China*

³*Center for Astrophysics, Guangzhou University, Guangzhou 510006, China*

⁴*School of Physical Science and Technology, Kunming University 650214, P. R. China*

⁵*School of mathematics and physics, Anqing Normal University 246011, P. R. China*

⁶*Yunnan Observatories, Chinese Academy of Sciences, Kunming 650011, China*

Accepted XXX. Received YYY; in original form ZZZ

ABSTRACT

We calculate the jet power of the Blandford-Znajek (BZ) model and the hybrid model based on the self-similar solution of advection-dominated accretion flows (ADAFs). We study the formation mechanism of the jets of BL Lacs with known redshifts detected by the Fermi satellite after 10 yr of data (4FGL-DR2). The kinetic power of the jets of Fermi BL Lacs is estimated through radio luminosity. The main results are as follows. (1) We find that the jet kinetic power of about 72% intermediate peak frequency BL Lacs (IBL) and 94% high-frequency peak BL Lacs (HBL) can be explained by the hybrid jet model based on ADAFs surrounding Kerr black holes. However, the jet kinetic power of about 74% LBL cannot be explained by the BZ jet model or the hybrid model. (2) The LBL has a higher accretion rate than IBL and HBL. About 14% IBL and 62% HBL have pure optically thin ADAFs. However, 7% LBL may have a hybrid structure consisting of an standard thin disk (SS) plus optically thin ADAFs. (3) After excluding the redshift dependence, there is a weak correlation between the jet kinetic power and the accretion disk luminosity for Fermi BL Lacs. (4) There is a significant correlation between inverse Compton luminosity and synchrotron luminosity for Fermi BL Lacs. The slope of the relation between inverse Compton luminosity and synchrotron luminosity for Fermi BL Lacs is consistent with the synchrotron self-Compton (SSC) process. The result may suggest that the high-energy components of Fermi BL Lacs are dominated by the SSC process.

Key words: galaxies:active–BL Lacertae objects:general–galaxies:jets–gamma-rays:general

1 INTRODUCTION

BL Lacertae objects (BL Lacs) are a subclass of the blazar, an extreme type of active galactic nuclei (AGN), whose jets point to observer (e.g., Blandford & Rees 1978). The difference between BL Lacs and their sibling flat-spectrum radio quasars (FSRQs) is that the spectra of BL Lacs lack emission lines with an equivalent width less than 5 Å (e.g., Urry & Padovani 1995). BL Lacs usually have only weak or non-existent emission lines. The lack of strong emission lines may be attributed to an ineffective accretion process, which does not produce sufficient energy to photoionize the broad line region (BLR) clouds (e.g., Ghisellini et al. 2011; Sbarato et al. 2014). Ghisellini et al. (2011) found that the BL Lacs have a low ratio of the luminosity of the broad-line region (BLR) to the Eddington luminosity, $L_{\text{BLR}}/L_{\text{Edd}} \leq 5 \times 10^{-4}$. Sbarato et al. (2014) also found that the BL Lacs have $L_{\text{BLR}}/L_{\text{Edd}} < 10^{-3}$. These results show that the BL Lacs have a low accretion rate.

According to the frequency at which the synchrotron component of the spectral energy distribution (SED) peaks, BL Lacs can be divided into different subcategories, namely, low-frequency peak BL Lacs (LBL), intermediate peak frequency BL Lacs (IBL) and high-frequency peak BL Lacs (HBL; Padovani & Giommi (1996)), and set the boundaries as $\log \nu_p < 14$ Hz for LBL, $14 \text{ Hz} < \log \nu_p < 15$ Hz for IBL, and $\log \nu_p > 15$ Hz for HBL (e.g., Abdo et al. 2010). Since July 2008, the large area telescope on the Fermi Gamma-Ray Space Telescope (LAT, Atwood et al. (2009)) has scanned the entire gamma-ray sky about every three hours. Many blazars have been detected to have high-energy gamma-ray emissions, and the research of blazars has entered a new era. The LAT AGN catalog shows that the BL Lacs are the largest group of γ -ray sources (Abdollahi et al. 2020; Ajello et al. 2020). The most recent LAT AGN catalog contains 1207 BL Lacs (4FGL-DR2, Abdollahi et al. (2020); Ajello et al. (2020); Foschini et al. (2022)), which makes it possible to study the physical properties of a γ -ray selected sample of BL Lacs. Li et al. (2010) studied the relationship between optical-to-X-ray (α_{ox}) and X-ray-to- γ -ray (α_{xy}) composite spectral indices and found that FSRQs

* E-mail: ynkmcyy@yeah.net

† E-mail: qsgu@nju.edu.cn

and LBL occupy the same region by using 54 Fermi blazars. They suggested that FSRQs and LBL have similar spectral properties.

By now, several questions have been raised about BL Lacs, for example, what is the formation mechanism of the jets of BL Lacs? There are three theories of jet formation. The first is the Blandford-Znajek (BZ) mechanism (Blandford & Znajek 1977), in which jets extract the rotational energy of black holes. The second is the Blandford-Payne (BP) mechanism (Blandford & Payne 1982), in which the jet extracts the rotational energy of the accretion disk. In the above two cases, it should be maintained by matter accreting on the black hole, which leads to an expected relationship between accretion disk luminosity and jet power (Maraschi & Tavecchio 2003). Many authors have confirmed this relationship (e.g., Rawlings & Saunders 1991; Cao & Jiang 1999; Wang et al. 2004; Ghisellini et al. 2009; Gu et al. 2009; Ghisellini et al. 2010, 2011; Sbarrato et al. 2012, 2014; Xiong & Zhang 2014; Chen et al. 2015b; Paliya et al. 2017, 2019; Xiao et al. 2022; Zhang et al. 2022). The third is the hybrid model, that is, the combination of BZ and BP mechanisms (Meier 1999, 2001; Garofalo et al. 2010). Garofalo et al. (2010) used a hybrid model to speculate the differences observed in AGN with relativistic jets. Cao (2003) calculated the maximal jet power of BP mechanism and BZ mechanism for a standard thin accretion disk. Comparing with the jet kinetic power of 29 BL Lacs, they found that the BZ and BP mechanisms could not explain the jet kinetic power of BL Lacs. These results imply that the accretion disks in most BL Lacs should not be standard accretion disks. Deng et al. (2021) used the one-zone Leptonic jet model to get the jet kinetic power of two HBLs (Mrk 421 and Mrk 501). Compared with the maximum jet power of the BZ mechanism and the BP mechanism for a thin disk, they found that the BZ mechanism may explain the jet kinetic power of Mrk 421, while the jet kinetic power of Mrk 501 may be explained by the BP mechanism or the BZ mechanism. Xiao et al. (2022) found a significant correlation between jet power and normalized disk luminosity ($L_{\text{disk}}/L_{\text{Edd}}$) for 16 BL Lacs. They suggested that the jet powers of 16 BL Lacs are powered by BZ mechanism. Although there are some studies on the jet mechanism of BL Lacs, however, no author has used a large sample of BL Lacs to study their jet mechanism in the case of ADAFs.

The SED contains two emission components, namely the synchrotron component and inverse Compton (IC) component (e.g., Ghisellini et al. 1997; Massaro et al. 2004, 2006). In the Leptonic model, it is generally believed that the low energy peak is generated by the synchrotron emission of relativistic electrons from the jet and the high energy peak is generated by IC scattering (e.g., Massaro et al. 2004, 2006; Meyer et al. 2012). However, there are disagreements regarding the origin of soft photons scattered by IC. (1) They come from synchrotron emission, called synchrotron self Compton (SSC) process (e.g., Rees 1967; Jones et al. 1974; Marscher & Gear 1985; Maraschi et al. 1992; Sikora et al. 1994; Bloom & Marscher 1996). (2) They come from the outside of the jet, called the external Compton (EC) process. There are three possible sources of EC soft photons: accretion disk photons entering the jets directly (Dermer et al. 1992; Dermer & Schlickeiser 1993); broad-line region (BLR) photons entering the jets (Sikora et al. 1994; Dermer et al. 1997); and infrared radiation photons from the dust torus entering the jet (Blažejowski et al. 2000; Arbeiter et al. 2002). Ghisellini (1996) obtains two relationships between synchrotron luminosity and IC luminosity, which determines whether the IC component is dominated by the EC process or the SSC process ($L_{\text{EC}} \sim L_{\text{syn}}^{1.5}$, $L_{\text{SSC}} \sim L_{\text{syn}}^{1.0}$).

In this work, we study the physical properties of the jets of BL Lacs. Section 2 describes the sample. Section 3 is the jet model. In Section 4, we describe the results and discussion. Section 5 is the con-

clusion. Throughout this article, a standard concordance cosmology was assumed ($H_0 = 70 \text{ km s}^{-1}\text{Mpc}^{-1}$, $\Omega_M = 1 - \Omega_A = 0.27$).

2 THE FERMI BL LACS SAMPLE

We try to select a large sample of Fermi BL Lacs with reliable redshift, black hole mass, and accretion disk luminosity. For this, we consider the sample of Paliya et al. (2021), who used 1077 blazars detected with the Fermi Large Area Telescope (4FGL-DR2) to study the central engines of Fermi blazars.

2.1 The black hole mass

For the case of BL Lac objects that lack strong broad emission lines, Paliya et al. (2021) obtained the black hole mass (M_{BH}) through the following two methods.

First, the black hole mass is calculated by using the stellar velocity dispersion (σ_*). The formula is as follows (Gültekin et al. 2009),

$$\log \left(\frac{M_{\text{BH}}}{M_{\odot}} \right) = (8.12 \pm 0.08) + (4.24 \pm 0.41) \times \log \left(\frac{\sigma_*}{200 \text{ km s}^{-1}} \right). \quad (1)$$

Second, Paliya et al. (2021) used the bulge luminosity to estimate the black hole mass. The formula is as follows (Graham 2007),

$$\log \left(\frac{M_{\text{BH}}}{M_{\odot}} \right) = \begin{cases} (-0.38 \pm 0.06)(M_R + 21) + (8.11 \pm 0.11), \\ (-0.38 \pm 0.06)(M_K + 24) + (8.26 \pm 0.11). \end{cases} \quad (2)$$

where M_R and M_K are the absolute magnitudes of the host galaxy bulge in the R and K bands, respectively.

We also note that the black hole mass of our sample is obtained by different methods. The uncertainty of the black hole mass estimated by stellar velocity dispersion is small, ≤ 0.25 dex. The uncertainty of the black hole mass estimated by the bulge luminosity is 0.6 dex.

2.2 The accretion disk luminosity

Due to the lack of detection of emission lines, it is impossible to use emission lines to infer the BLR luminosity. Therefore, Paliya et al. (2021) derived a 3σ upper limit in the $\text{H}\beta$ (or Mg II , depending on the source redshift and wavelength coverage) line luminosity. Paliya et al. (2021) calculated the BLR luminosity by scaling several strong emission lines to the quasar template spectrum of Francis et al. (1991) and Celotti et al. (1997), using $\text{Ly}\alpha$ as a reference and giving the total BLR fraction $< L_{\text{BLR}} > = 555.77$. The BLR luminosity is estimated through the following formula,

$$L_{\text{BLR}} = L_{\text{line}} \times \frac{< L_{\text{BLR}} >}{L_{\text{ref.frac}}}, \quad (3)$$

where L_{line} is the emission-line luminosity and $L_{\text{ref.frac}}$ is the ratio: 22 and 34 for $\text{H}\beta/\text{Ly}\alpha$ and $\text{Mg II}/\text{Ly}\alpha$ (Francis et al. 1991; Celotti et al. 1997), respectively. When more than one line luminosity measurements were available, Paliya et al. (2021) took their geometric mean to derive the average L_{BLR} . The accretion disk luminosity is estimated by using $L_{\text{disk}} = 10L_{\text{BLR}}$ (e.g., Baldwin & Netzer 1978), with an average uncertainty of a factor 2 (Calderone et al. 2013; Ghisellini et al. 2014).

We carefully examined the samples of Paliya et al. (2021) and compared them with the classification of the sources of Abdollahi et al. (2020) and Foschini et al. (2022). We only consider that these sources with 1.4 GHz radio flux comes from the The FIRST Survey

Catalog (Becker et al. 1995): 14Dec17 Version¹. Finally, we get 276 Fermi BL Lacs (57 LBL, 43 IBL, and 176 HBL). The relevant data is listed in Table 1.

2.3 The jet kinetic power

Komossa et al. (2018) used the following formula to estimate the jet kinetic power (P_{kin}) in AGN (Bîrzan et al. 2008)

$$\log P_{\text{kin}} = 0.35(\pm 0.07) \log P_{1.4} + 1.85(\pm 0.10) \quad (4)$$

where P_{kin} is in units of 10^{42} erg s $^{-1}$, and $P_{1.4}$ is the 1.4 GHz radio luminosity in units of 10^{40} erg s $^{-1}$, $P_{1.4} = 4\pi d_L^2 \nu S_\nu$. The scatter for this relation is $\sigma = 0.85$ dex. We make a K-correction for the observed flux using $S_\nu = S_\nu^{\text{obs}}(1+z)^{\alpha-1}$, where α is the spectral index and ν is the frequencies, and $\alpha = 0$ is adopted (Abdo et al. 2010; Komossa et al. 2018). The S_ν^{obs} is the observed flux. The d_L is the distance of luminosity, $d_L(z) = \frac{c}{H_0}(1+z)\int_0^z [\Omega_A + \Omega_M(1+z')^3]^{-1/2} dz'$ (Venters et al. 2009). Most galaxies have a central supermassive black hole, which may coevolve with the host galaxy, resulting in correlations between bulge luminosity, stellar velocity dispersion, and central black hole mass (e.g., Kormendy & Richstone 1995; Magorrian et al. 1998). Models show that these correlations are caused by galaxy merging and feedback from AGN (e.g., Silk & Rees 1998; Kauffmann & Haehnelt 2000). Around the time of these discoveries, the Chandra X-ray observation found direct evidence of AGN feedback, when observations revealed cavities and shock fronts in X-ray emission gas around many massive galaxies (e.g., Fabian et al. 2000; McNamara et al. 2000). The X-ray cavity provides a direct measurement of the mechanical energy released by the AGN through the work done on the hot, gaseous halo around them (McNamara et al. 2000). This energy is expected to heat the gas and prevent it from cooling and forming stars (Churazov et al. 2001). Studies on X-ray cavities show that AGN feedback provides enough energy to regulate star formation and inhibit the cooling of the hot halos of galaxies and clusters (e.g., Bîrzan et al. 2008; Komossa et al. 2018). Komossa et al. (2018) believes that if the relationship of Cavagnolo et al. (2010) is used to calculate jet kinetic power, the high value of jet kinetic power is predicted up to an order of magnitude. At the same time, all of our samples have a 1.4 GHz radio flux, but there is almost no low-frequency radio flux (for example 150 MHz). We cannot use low-frequency radio flux to calculate jet kinetic power. Therefore, we follow the method of Komossa et al. (2018) and use equation (1) to calculate the jet kinetic power. We note that the total jet power (P_{jet}) is given by the sum of two components i.e., the radiation power (P_{rad}) and the kinetic power (P_{kin}). The jet power of radiation is believed to be about 10% of the jet kinetic power (Nemmen et al. 2012; Ghisellini et al. 2014), namely $P_{\text{kin}} \sim 10P_{\text{rad}}$. Since the total jet power is mainly dominated by the jet kinetic power, the value of the total jet power can be approximately equal to the jet kinetic power.

3 JET MODEL

Currently, the most popular theories of jet formation include the BZ mechanism (Blandford & Znajek 1977) and the BP mechanism (Blandford & Payne 1982). Recently, some authors have proposed a hybrid jet model (Meier 1999; Garofalo et al. 2010), that is, the

mixture of BZ and BP. Theoretical works on jet power computation in the case of ADAF are often based on the self-similar solution of ADAFs of Narayan & Yi (1995), Meier (2001), and Nemmen et al. (2007). There is some evidence to suggest that accretion flows on low accretion rate AGN (or low jet power, such as BL Lacs, low/hard-state X-ray binaries, and radio galaxies) are best described as ADAFs (e.g., Wu & Cao 2008; Wu et al. 2011). In addition, the magnitude and structure of the magnetic field related to ADAFs are more favorable for extracting spin energy from the black hole than the magnetic field related to the standard thin disk (e.g., Livio et al. 1999; Nemmen et al. 2007). The BZ phenomenon is the backbone of the jet, and as the accretion increases, the BZ phenomenon becomes increasingly hybridized (Cavaliere & D'Elia 2002). The jet mechanism becomes hybridized as the accretion rate increases. Tombesi et al. (2010) found that some relatively highly accreting radio galaxies have ultra-fast outflows with $v \sim (0.04 - 0.15)c$. Although these winds move at relativistic speeds, their findings indicate that some hydromagnetic windy activity is also present in AGNs with relativistic jets, thus enforcing the idea of a hybrid mechanism (Foschini 2011). At the same time, our sample has a low accretion rate (see below), which implies that these sources may have ADAFs. Therefore, in this work, we calculate the jet power based on the self-similar solution of ADAFs around the Kerr black hole.

3.1 The BZ jet model

The jet power of BZ mechanism ($P_{\text{jet}}^{\text{BZ}}$) is estimated by the following formula (MacDonald & Thorne 1982; Thorne et al. 1986; Ghosh & Abramowicz 1997; Nemmen et al. 2007)

$$P_{\text{jet}}^{\text{BZ}} = \frac{1}{32}\omega_F^2 B_\perp^2 R_H^2 j^2 c, \quad (5)$$

where $\omega_F \equiv \Omega_F(\Omega_H - \Omega_F)/\Omega_H^2$ depends on the angular velocity of field lines Ω_F relative to that of the black hole Ω_H . We assume $\omega_F = 1/2$, which implies the output of maximum power (e.g., MacDonald & Thorne 1982; Thorne et al. 1986; Nemmen et al. 2007). The B_\perp is assumed to approximate to the poloidal component of the magnetic field B_p , $B_\perp \approx B_p(R_{\text{ms}}) \approx g(R_{\text{ms}})B(R_{\text{ms}})$ (Livio et al. 1999), $g = \Omega/\Omega'$. The R_{ms} is the radius of the marginally stable orbit of the accretion disk (see APPENDIX A). The Ω' is the angular velocity of the disk. An observer at infinity will see the disk and the magnetic fields near the black hole rotate, in the Boyer–Lindquist coordinate system, not with an angular velocity Ω' but $\Omega = \Omega' + \omega$ (Bardeen et al. 1972), where ω is the angular velocity of the local metric which is given in Appendix A, equation (A11). The B is the magnetic field strength near the black hole (see APPENDIX A). The $R_H = [1 + (1 - j^2)^{1/2}]GM_{\text{BH}}/c^2$ is the horizon radius (e.g., Ghosh & Abramowicz 1997), where G is the gravitational constant and M is the mass of the black hole. The j is spin of black hole and c is the speed of light.

3.2 The Hybrid jet model

The jet power of the hybrid model ($P_{\text{jet}}^{\text{Hybrid}}$) is estimated by the following formula (Meier 2001; Nemmen et al. 2007)

$$P_{\text{jet}}^{\text{Hybrid}} = (B_\phi H R \Omega)^2 / 32c, \quad (6)$$

where B_ϕ is the azimuthal component of the magnetic field. Meier (2001) related the amplified, azimuthal component of the magnetic

¹ <http://sundog.stsci.edu/first/catalogs/readme.html>

Table 1. The sample of Fermi BL Lacs.

4FGL name (1)	RA (2)	DEC (3)	Type (4)	Redshift (5)	log M (6)	log L_{disk} (7)	f_{ν} (8)	log P_{kin} (9)	log L_{sy} (10)	log L_{ic} (11)
J0003.2+2207	0.8058	22.1302	HBL	0.1	8.10	42.74	0.0087	43.84	43.23	42.55
J0006.3-0620	1.5992	-6.3493	LBL	0.347	8.92	44.52	2.051	45.12	45.74	44.79
J0013.9-1854	3.4804	-18.9118	HBL	0.095	9.65	43.27	0.0295	44.01	44.02	42.94
J0014.1+1910	3.5368	19.1713	LBL	0.477	7.47	44.32	0.154	44.86	45.46	45.61
J0014.2+0854	3.5695	8.9114	HBL	0.163	8.85	43.37	0.326	44.55	43.75	43.38
J0015.6+5551	3.9071	55.8636	HBL	0.217	9.68	44.05	0.0849	44.45	44.67	44.21
J0017.8+1455	4.4711	14.9228	IBL	0.303	8.27	44.16	0.0595	44.52	44.84	44.53
J0021.6-0855	5.4115	-8.9174	IBL	0.648	8.54	44.63	0.0472	44.82	45.33	45.43
J0022.0+0006	5.5154	0.1134	HBL	0.306	8.02	43.79	0.0042	44.13	44.57	44.06
J0032.4-2849	8.1076	-28.8224	LBL	0.324	8.47	44.02	0.161	44.70	44.95	45.05
J0040.4-2340	10.1012	-23.6704	IBL	0.213	8.68	43.75	0.0536	44.38	44.00	43.74
J0045.7+1217	11.4309	12.292	HBL	0.255	8.82	44.18	0.104	44.54	44.78	44.65
J0049.0+2252	12.252	22.8735	IBL	0.264	9.04	43.63	0.076	44.51	44.09	43.88
J0056.3-0935	14.0874	-9.5997	HBL	0.103	8.96	43.22	0.201	44.32	43.92	43.52
J0059.3-0152	14.8361	-1.8725	HBL	0.144	8.63	43.52	0.018	44.07	44.15	43.68
J0103.5+1526	15.8786	15.4348	IBL	0.246	9.02	43.78	0.226	44.65	44.25	43.94
J0103.8+1321	15.969	13.3536	HBL	0.49	9.69	44.41	0.0519	44.70	45.33	44.92
J0105.1+3929	16.2913	39.4963	LBL	0.44	8.17	44.34	0.0915	44.74	45.76	46.05
J0111.4+0534	17.8573	5.5761	HBL	0.347	8.47	44.06	0.0165	44.38	44.82	43.97
J0115.8+2519	18.9539	25.3324	HBL	0.376	9.03	44.53	0.0382	44.54	45.31	45.16
J0127.9+4857	21.9777	48.9536	LBL	0.065	7.23	42.92	0.206	44.18	43.95	43.65
J0137.9+5814	24.4957	58.2494	HBL	0.275	9.55	44.32	0.171	44.65	45.18	44.78
J0139.0+2601	24.7581	26.0298	IBL	0.347	8.10	44.25	0.129	44.70	44.78	44.37
J0146.9-5202	26.729	-52.0477	IBL	0.098	9.17	43.41	1.07	44.56	43.63	43.28
J0148.2+5201	27.0594	52.0243	HBL	0.437	9.75	44.74	0.0444	44.63	45.77	45.15
J0151.3+8601	27.8381	86.0194	IBL	0.15	9.25	43.54	0.0959	44.34	44.13	44.06
J0152.6+0147	28.1614	1.7894	HBL	0.08	9.34	42.92	0.0619	44.06	44.24	43.54
J0201.1+0036	30.2779	0.6029	HBL	0.298	8.19	43.93	0.0132	44.29	44.88	44.03
J0203.7+3042	30.9327	30.7139	LBL	0.761	8.41	45.01	0.175	45.10	46.32	46.69
J0204.0-3334	31.0238	-33.5731	HBL	0.617	9.29	44.34	0.0063	44.49	45.84	45.06
J0209.9+7229	32.4979	72.4877	LBL	0.895	7.76	45.12	0.67	45.39	46.54	46.89
J0219.1-1724	34.7821	-17.402	HBL	0.128	8.61	43.35	0.0625	44.22	44.10	43.36
J0227.3+0201	36.8296	2.0203	HBL	0.457	9.47	44.52	0.0368	44.62	45.25	45.12
J0232.8+2018	38.2139	20.3159	HBL	0.139	10.08	43.18	0.0834	44.29	44.60	43.81
J0237.6-3602	39.4244	-36.0422	HBL	0.411	8.31	44.66	0.0271	44.53	45.43	44.88
J0238.6+1637	39.668	16.6179	LBL	0.94	8.58	45.30	1.94	45.58	47.45	47.88
J0250.6+1712	42.6563	17.2081	HBL	0.243	9.47	44.23	0.07	44.47	44.84	44.51
J0304.5-0054	46.1423	-0.9148	HBL	0.511	9.16	44.68	0.0233	44.60	45.34	44.77
J0305.1-1608	46.2919	-16.1466	HBL	0.311	9.24	44.10	2.71	45.12	44.68	44.56
J0325.5-5635	51.3794	-56.591	HBL	0.06	9.10	42.84	0.0736	44.00	43.42	42.90
J0326.2+0225	51.5724	2.4228	HBL	0.147	9.21	43.51	0.0682	44.28	44.42	44.09
J0334.2-4008	53.5566	-40.145	LBL	1.359	8.67	44.66	1.92	45.81	47.85	48.10
J0338.1-2443	54.5305	-24.7207	HBL	0.251	9.72	43.73	0.0139	44.23	44.46	43.67
J0339.2-1736	54.8119	-17.6003	HBL	0.066	8.98	43.39	0.171	44.15	43.70	43.17
J0403.5-2437	60.8989	-24.6168	LBL	0.357	9.75	43.84	0.167	44.75	45.07	44.88
J0407.5+0741	61.8921	7.6998	LBL	1.139	8.84	45.33	0.296	45.41	46.89	47.32
J0416.9+0105	64.2269	1.088	HBL	0.287	8.40	44.15	0.121	44.61	45.64	44.67
J0420.2+4012	65.0547	40.201	HBL	0.132	9.35	43.77	0.116	44.32	43.85	43.46
J0428.6-3756	67.173	-37.9403	LBL	1.11	8.77	44.90	0.737	45.53	47.52	48.32
J0433.6+2905	68.4107	29.0975	LBL	0.91	8.25	44.93	0.154	45.18	46.02	47.12
J0505.8-3817	76.4749	-38.2965	HBL	0.182	9.01	43.91	0.019	44.16	44.06	43.63
J0516.7-6207	79.1798	-62.1248	LBL	1.3	8.67	45.17	0.418	45.55	47.47	47.77
J0538.8-4405	84.7089	-44.0862	LBL	0.896	8.45	46.22	2.89	45.62	47.81	48.01
J0558.0-3837	89.5233	-38.6317	HBL	0.302	9.81	44.52	0.106	44.61	45.56	44.80
J0629.3-1959	97.3478	-19.9999	LBL	1.718	9.88	45.83	0.677	45.82	48.36	48.37
J0640.0-1253	100.0213	-12.896	HBL	0.137	9.91	44.02	0.225	44.44	44.74	43.96
J0648.7+1516	102.1905	15.2808	HBL	0.179	8.84	44.12	0.0647	44.34	44.97	44.79
J0654.7+4246	103.6856	42.7791	LBL	0.129	7.55	43.02	0.203	44.40	43.77	43.75

Table 1 – continued .

4FGL name (1)	RA (2)	DEC (3)	Type (4)	Redshift (5)	log M (6)	log L_{disk} (7)	f_{ν} (8)	log P_{kin} (9)	log L_{sy} (10)	log L_{ic} (11)
J0656.3+4235	104.0918	42.5936	HBL	0.059	9.86	42.93	0.934	44.38	43.19	42.55
J0709.1+2241	107.2769	22.6847	HBL	0.297	9.72	44.39	0.0406	44.46	45.07	44.85
J0710.4+5908	107.6234	59.1352	HBL	0.125	9.75	42.75	0.159	44.35	44.73	44.08
J0710.9+4733	107.7323	47.553	LBL	1.292	8.81	45.70	1.02	45.68	47.01	47.73
J0731.9+2805	112.981	28.0882	HBL	0.248	8.58	43.92	0.0721	44.48	44.56	43.94
J0740.9+3203	115.2335	32.0581	IBL	0.179	8.46	43.53	0.077	44.37	44.04	43.61
J0744.1+7434	116.0345	74.5778	HBL	0.315	9.94	44.15	0.0233	44.40	45.40	44.78
J0749.2+2314	117.3217	23.2337	HBL	0.174	8.71	43.36	0.0547	44.31	43.99	43.47
J0758.9+2703	119.7258	27.0653	IBL	0.099	8.50	43.08	0.0691	44.15	43.50	43.39
J0803.2-0337	120.8247	-3.6189	HBL	0.365	6.96	43.95	0.232	44.81	44.91	45.24
J0809.6+3455	122.4215	34.9252	HBL	0.082	8.80	43.00	0.223	44.26	43.83	42.99
J0809.8+5218	122.4617	52.3143	HBL	0.138	8.55	43.85	0.183	44.41	44.96	44.63
J0811.4+0146	122.861	1.7756	LBL	1.148	8.71	44.98	0.599	45.52	47.09	47.43
J0812.0+0237	123.0094	2.6285	HBL	0.173	9.66	43.57	0.123	44.43	44.21	44.04
J0814.4+2941	123.6104	29.6857	LBL	0.374	8.58	44.96	0.0047	44.22	44.54	44.81
J0818.4+2816	124.6076	28.2738	IBL	0.225	8.09	43.97	0.064	44.42	44.50	44.02
J0820.9+2353	125.2255	23.89	HBL	0.402	8.46	44.26	0.0487	44.61	44.99	44.88
J0823.3+2224	125.8443	22.4093	LBL	0.951	7.96	44.13	2.27	45.61	46.70	46.37
J0828.3+4152	127.0877	41.879	HBL	0.154	8.58	43.68	0.091	44.34	44.05	43.36
J0829.0+1755	127.2747	17.9233	HBL	0.089	8.38	42.92	0.336	44.35	43.62	42.91
J0831.8+0429	127.9732	4.4941	LBL	0.174	7.00	43.48	1.24	44.78	45.10	45.01
J0832.4+4912	128.1078	49.2127	LBL	0.548	8.07	44.17	0.344	45.04	45.88	45.92
J0837.3+1458	129.3461	14.9677	HBL	0.152	7.74	43.43	0.0541	44.26	44.65	43.30
J0842.5+0251	130.6331	2.8662	HBL	0.425	8.27	44.32	0.0168	44.47	44.94	44.56
J0847.2+1134	131.8119	11.5692	HBL	0.198	8.04	43.75	0.0332	44.28	44.95	44.44
J0850.5+3455	132.6378	34.9285	HBL	0.145	8.67	43.82	0.0312	44.16	43.89	43.54
J0854.0+2753	133.5155	27.884	HBL	0.494	8.52	44.32	0.0144	44.51	44.92	44.08
J0901.4+4542	135.3691	45.707	IBL	0.288	7.83	43.89	0.021	44.35	44.40	44.10
J0909.7+3104	137.4477	31.0818	HBL	0.272	8.91	43.96	0.196	44.66	44.85	43.98
J0910.8+3859	137.7091	38.9999	IBL	0.199	7.73	43.76	0.0103	44.10	44.41	43.88
J0912.9-2102	138.2274	-21.0446	HBL	0.198	9.53	43.93	0.329	44.63	45.16	44.53
J0916.7+5238	139.1906	52.6454	IBL	0.19	8.60	43.66	0.139	44.48	44.44	43.76
J0917.3-0342	139.3339	-3.7035	HBL	0.308	9.34	44.09	0.0321	44.44	44.81	44.25
J0930.5+4951	142.6254	49.8577	HBL	0.187	8.87	43.64	0.0214	44.19	44.73	43.90
J0932.7+1041	143.1802	10.6903	HBL	0.361	9.16	44.12	0.0336	44.51	44.90	44.53
J0940.4+6148	145.1207	61.8156	HBL	0.211	8.63	43.66	0.0128	44.15	44.43	43.96
J0942.3+2842	145.5806	28.7091	HBL	0.366	8.60	43.92	0.022	44.45	44.25	44.18
J0945.7+5759	146.432	57.9871	IBL	0.229	8.62	43.90	0.112	44.51	44.64	44.15
J0946.2+0104	146.5672	1.0701	HBL	0.128	7.70	43.43	0.154	44.36	43.88	43.45
J0955.1+3551	148.7816	35.8584	HBL	0.557	8.92	44.44	0.0078	44.47	45.53	44.67
J0959.4+2120	149.8712	21.3459	HBL	0.365	8.28	44.16	0.0408	44.54	45.27	44.48
J1001.1+2911	150.2938	29.188	LBL	0.556	7.78	44.68	0.146	44.92	46.01	45.95
J1010.2-3119	152.5716	-31.3207	HBL	0.143	9.97	43.57	0.0743	44.28	44.66	44.02
J1023.8+3002	155.9608	30.0458	HBL	0.433	9.06	44.43	0.009	44.38	45.01	44.75
J1026.9+0608	156.7322	6.1431	HBL	0.449	9.20	44.40	0.0105	44.42	45.28	44.75
J1031.1+7442	157.7925	74.7019	LBL	0.123	7.87	43.88	0.209	44.39	44.18	44.22
J1031.3+5053	157.8454	50.8839	HBL	0.36	8.07	44.14	0.0379	44.52	45.83	45.41
J1033.5+4221	158.3827	42.3507	HBL	0.211	8.65	43.52	0.0448	44.35	43.90	43.41
J1035.6+4409	158.9225	44.1609	IBL	0.444	7.76	44.06	0.0429	44.63	44.47	45.02
J1041.7+3902	160.4411	39.0426	HBL	0.208	8.73	43.74	0.0223	44.23	44.05	43.62
J1041.9-0557	160.4774	-5.9528	HBL	0.39	8.54	44.18	0.0836	44.68	45.24	44.70
J1043.2+2408	160.8053	24.146	LBL	0.559	8.63	44.89	0.325	45.04	46.02	45.94
J1046.8-2534	161.7027	-25.5749	HBL	0.254	9.94	43.77	0.0141	44.24	44.97	44.25
J1049.5+1548	162.3892	15.8086	IBL	0.326	8.25	44.41	0.0506	44.53	45.09	44.86
J1049.7+5011	162.4334	50.1836	HBL	0.402	8.49	44.01	0.0078	44.33	44.80	44.45
J1051.4+3942	162.8702	39.7159	HBL	0.497	9.10	44.48	0.0108	44.47	45.56	45.03
J1051.9+0103	162.9886	1.0647	IBL	0.265	7.61	43.69	0.0163	44.28	44.14	43.80
J1053.7+4930	163.4253	49.5081	HBL	0.14	8.74	43.46	0.0646	44.26	44.16	43.61
J1057.8-2754	164.454	-27.9016	HBL	0.091	9.36	43.69	0.0638	44.11	43.74	43.06
J1058.4+0133	164.624	1.5641	LBL	0.892	9.50	45.74	3.22	45.63	47.26	47.48

Table 1 – continued .

4FGL name (1)	RA (2)	DEC (3)	Type (4)	Redshift (5)	log M (6)	log L_{disk} (7)	f_{ν} (8)	log P_{kin} (9)	log L_{sy} (10)	log L_{ic} (11)
J1058.6+5627	164.6652	56.4634	HBL	0.143	8.33	43.90	0.229	44.46	44.81	44.55
J1058.6-8003	164.66	-80.064	LBL	0.581	8.64	45.49	0.77	45.19	46.37	46.35
J1104.4+3812	166.1187	38.207	HBL	0.033	9.05	42.18	0.769	44.16	44.62	44.51
J1105.8+3944	166.4589	39.7426	LBL	0.099	8.29	42.67	0.045	44.08	43.71	42.86
J1109.6+3735	167.4092	37.5868	HBL	0.398	8.96	44.16	0.0044	44.24	44.79	44.59
J1112.4+1751	168.1132	17.8509	HBL	0.421	8.46	44.45	0.0143	44.44	45.24	44.73
J1117.0+2013	169.2708	20.2294	HBL	0.138	8.51	43.71	0.103	44.32	44.52	44.43
J1119.6-3047	169.9245	-30.7962	HBL	0.412	9.75	44.03	0.0094	44.37	44.84	44.48
J1124.4+2308	171.102	23.137	LBL	0.795	7.86	44.87	0.154	45.10	45.55	45.88
J1125.5-3557	171.3929	-35.9581	LBL	0.284	7.28	43.55	0.208	44.69	44.87	44.82
J1130.5-3137	172.6499	-31.6219	HBL	0.151	9.24	43.43	0.0265	44.15	43.92	43.64
J1130.8+1016	172.7192	10.2728	IBL	0.172	8.41	44.01	0.0136	44.09	44.23	44.11
J1131.4+5809	172.8555	58.151	IBL	0.36	8.42	44.21	0.0444	44.55	45.19	44.94
J1136.4+6736	174.1179	67.6127	HBL	0.134	8.67	43.49	0.0458	44.19	44.56	44.10
J1136.8+2550	174.2171	25.8463	HBL	0.154	9.46	43.53	0.0163	44.08	44.31	43.20
J1140.5+1528	175.129	15.4824	HBL	0.244	8.70	43.97	0.07	44.47	44.98	44.02
J1147.0-3812	176.76	-38.2006	LBL	1.053	8.69	45.38	1.8	45.64	47.27	47.31
J1149.4+2441	177.3713	24.6873	HBL	0.402	8.21	44.32	0.00758	44.33	45.70	44.62
J1152.1+2837	178.0309	28.6293	HBL	0.441	9.06	44.37	0.0246	44.54	45.20	44.67
J1153.7+3822	178.4464	38.3684	LBL	0.41	8.11	44.26	0.15	44.79	45.08	44.31
J1154.0-0010	178.5103	-0.1787	HBL	0.254	8.13	43.75	0.0106	44.19	44.65	44.19
J1202.4+4442	180.61	44.7147	IBL	0.297	8.80	44.11	0.106	44.60	44.40	44.24
J1203.1+6031	180.7881	60.518	IBL	0.065	8.40	43.20	0.191	44.17	43.84	43.18
J1203.4-3925	180.852	-39.4257	HBL	0.227	8.88	43.64	0.0646	44.43	44.24	44.22
J1204.0+1146	181.0204	11.7761	HBL	0.296	8.37	43.89	0.0151	44.31	45.01	44.46
J1212.0+2242	183.0146	22.709	HBL	0.453	8.16	44.50	0.0202	44.53	45.48	44.52
J1215.1+0731	183.7895	7.5222	HBL	0.136	8.89	43.49	0.138	44.36	44.04	43.48
J1216.1+0930	184.0415	9.5096	HBL	0.094	8.95	42.97	0.209	44.30	43.71	43.18
J1219.7-0313	184.9334	-3.2217	HBL	0.299	8.45	44.18	0.0289	44.41	44.77	44.63
J1221.3+3010	185.3449	30.1677	HBL	0.184	9.00	44.17	0.0715	44.37	45.19	45.10
J1221.5+2814	185.3784	28.2382	IBL	0.102	8.55	43.81	0.732	44.52	44.71	44.58
J1223.9-7954	185.9854	79.9025	HBL	0.375	9.53	44.32	0.0315	44.51	44.44	44.15
J1224.4+2436	186.1161	24.6142	HBL	0.219	8.29	44.11	0.0259	44.28	45.10	44.62
J1231.5+1421	187.8771	14.3532	IBL	0.256	8.73	44.07	0.05	44.43	44.59	44.38
J1231.6+6415	187.9012	64.2535	HBL	0.163	8.96	43.49	0.0588	44.29	44.26	43.80
J1233.6+5027	188.4105	50.4606	IBL	0.207	8.32	43.59	0.283	44.62	44.27	44.04
J1236.3+3858	189.0894	38.9814	IBL	0.389	8.54	44.15	0.037	44.55	44.79	44.49
J1237.8+6256	189.457	62.9342	HBL	0.297	8.64	43.86	0.0125	44.28	44.60	43.84
J1244.5+1616	191.1361	16.2803	HBL	0.456	8.76	44.23	0.154	44.84	44.78	44.77
J1246.3+0112	191.5786	1.2166	IBL	0.386	7.57	44.14	0.045	44.58	44.63	44.39
J1248.7+5127	192.1805	51.463	IBL	0.351	8.24	44.21	0.115	44.68	44.98	44.46
J1250.6+0217	192.6513	2.2876	LBL	0.954	8.69	45.08	0.341	45.33	46.22	46.43
J1251.2+1039	192.821	10.6536	IBL	0.245	7.62	43.89	0.154	44.59	44.44	44.10
J1254.9-4426	193.728	-44.4441	LBL	0.041	8.95	42.91	0.368	44.12	42.78	42.70
J1256.2-1146	194.0632	-11.7755	HBL	0.058	8.94	43.06	0.0544	43.94	43.53	42.99
J1257.6+2413	194.4191	24.2199	HBL	0.141	8.56	43.33	0.0147	44.03	44.19	43.15
J1258.3+6121	194.5879	61.3622	HBL	0.224	7.90	43.91	0.0102	44.14	43.95	43.77
J1319.5+1404	199.8979	14.0708	IBL	0.573	8.31	44.94	0.077	44.84	45.64	45.26
J1321.9+3219	200.4801	32.3313	IBL	0.396	8.73	43.90	0.0164	44.44	45.00	44.53
J1322.9+0437	200.7372	4.6308	HBL	0.224	8.94	43.70	0.037	44.34	44.36	43.93
J1326.1+1232	201.5493	12.5348	HBL	0.204	8.75	43.70	0.0574	44.37	44.50	43.72
J1331.0+5653	202.7577	56.894	HBL	0.27	8.63	43.75	0.00516	44.11	44.50	43.91
J1331.2-1325	202.8192	-13.4282	LBL	0.251	7.80	43.52	0.0512	44.43	44.26	45.01
J1335.3-2949	203.8475	-29.8295	HBL	0.513	9.78	44.32	0.0106	44.48	45.76	45.05
J1336.2+2320	204.051	23.3349	HBL	0.267	7.64	43.76	0.0134	44.25	44.46	44.02
J1340.8-0409	205.2171	-4.1612	HBL	0.223	9.60	43.96	0.027	44.29	44.46	44.13
J1341.2+3958	205.3209	39.9738	HBL	0.171	8.91	43.45	0.0878	44.37	44.52	43.71
J1341.6+5515	205.4087	55.254	HBL	0.207	8.17	43.56	0.0379	44.31	44.06	43.09
J1342.7+0505	205.6851	5.0904	IBL	0.136	8.56	43.37	1.6	44.73	44.57	43.90
J1351.9+2847	207.9959	28.7964	HBL	0.268	8.55	43.76	0.011	44.22	44.05	43.62

Table 1 – continued .

4FGL name (1)	RA (2)	DEC (3)	Type (4)	Redshift (5)	log M (6)	log L_{disk} (7)	f_{ν} (8)	log P_{kin} (9)	log L_{sy} (10)	log L_{ic} (11)
J1353.2+3740	208.3049	37.682	HBL	0.216	8.99	43.61	0.0343	44.31	44.35	43.81
J1353.4+5600	208.3602	56.0024	HBL	0.404	8.29	44.26	0.0149	44.43	44.89	44.30
J1402.6+1600	210.6584	16.0016	IBL	0.245	7.30	43.66	0.85	44.85	44.64	43.92
J1403.4+4319	210.8684	43.3225	HBL	0.493	8.16	44.27	0.0205	44.57	44.74	44.65
J1404.8+6554	211.2158	65.9048	HBL	0.363	8.41	44.26	0.0154	44.39	44.92	44.66
J1406.9+1643	211.742	16.7206	HBL	0.603	8.90	44.77	0.0083	44.52	45.89	45.28
J1410.3+1438	212.5908	14.6434	IBL	0.144	8.37	43.33	0.494	44.57	43.98	43.65
J1411.8+5249	212.9692	52.8278	HBL	0.076	8.82	42.78	0.848	44.44	43.43	42.63
J1412.1+7427	213.0383	74.45	IBL	0.436	6.35	43.45	0.107	44.76	44.93	45.28
J1415.5+4830	213.8992	48.5142	HBL	0.496	7.73	44.65	0.0287	44.62	45.27	45.03
J1416.1-2417	214.0334	-24.2982	HBL	0.136	9.21	43.48	0.0729	44.26	44.43	43.45
J1417.9+2543	214.494	25.7238	HBL	0.236	8.17	43.59	0.0887	44.49	45.30	44.42
J1419.8+5423	214.955	54.3937	LBL	0.152	9.12	44.17	0.789	44.66	45.15	44.42
J1424.1-1750	216.0294	-17.8447	HBL	0.082	8.59	43.27	0.013	43.83	43.43	42.90
J1428.5+4240	217.1286	42.6776	HBL	0.129	8.59	43.59	0.032	44.12	44.88	44.39
J1439.3+3932	219.8299	39.538	HBL	0.344	8.79	44.65	0.0442	44.53	45.50	44.86
J1440.9+0609	220.242	6.1631	HBL	0.396	9.49	43.35	0.0902	44.70	45.42	45.16
J1442.6-4623	220.6605	-46.3869	HBL	0.103	9.25	43.25	0.0964	44.21	44.13	43.38
J1442.7+1200	220.698	12.0126	HBL	0.163	8.74	43.64	0.06	44.30	44.77	44.06
J1443.6+2515	220.9028	25.2631	HBL	0.529	8.13	44.49	0.0067	44.43	45.21	44.94
J1503.5+4759	225.8955	47.9959	IBL	0.345	7.97	44.51	0.106	44.66	45.08	45.51
J1506.4+4331	226.6221	43.5257	IBL	0.47	9.03	44.37	0.0291	44.60	44.85	44.67
J1507.2+1721	226.8207	17.3519	HBL	0.565	8.19	44.48	0.0234	44.65	45.36	45.34
J1508.8+2708	227.2045	27.1407	HBL	0.27	8.30	43.95	0.0374	44.41	45.26	44.32
J1516.8+2918	229.2126	29.3123	IBL	0.13	8.79	43.24	0.0746	44.25	44.18	44.01
J1517.7-2422	229.4254	-24.373	LBL	0.048	9.09	43.15	2.04	44.43	44.19	43.93
J1518.6+4044	229.6606	40.7449	HBL	0.065	8.25	42.65	0.0409	43.93	43.25	42.72
J1523.2+0533	230.8241	5.5569	HBL	0.176	8.57	43.33	0.0362	44.25	44.08	43.42
J1532.0+3016	233.0159	30.2685	HBL	0.065	8.27	42.69	0.0544	43.97	43.48	42.99
J1533.2+1855	233.3103	18.9201	HBL	0.307	8.27	44.07	0.0229	44.38	45.12	44.57
J1534.8+3716	233.7218	37.2723	HBL	0.143	7.83	43.56	0.0224	44.10	44.01	43.60
J1535.4+3919	233.8741	39.3194	HBL	0.257	8.31	44.13	0.0197	44.29	44.92	44.05
J1540.7+1449	235.1903	14.822	LBL	0.606	8.23	44.18	1.39	45.30	46.09	45.96
J1541.7+1413	235.4469	14.2306	HBL	0.223	7.94	43.80	0.0354	44.33	44.75	43.96
J1548.3+1456	237.0999	14.9461	IBL	0.23	9.32	43.40	0.0244	44.28	44.40	44.81
J1558.9-6432	239.7377	-64.5404	HBL	0.08	8.94	43.39	0.94	44.48	44.08	43.59
J1605.5+5423	241.3848	54.3982	HBL	0.212	7.92	43.43	0.0076	44.08	44.31	43.90
J1606.3+5629	241.5917	56.4975	HBL	0.437	8.48	44.30	0.0157	44.47	45.41	44.80
J1616.7+4107	244.1821	41.1234	LBL	0.267	8.67	43.88	0.0958	44.55	44.69	44.61
J1626.3+3514	246.582	35.2382	HBL	0.498	8.82	44.47	0.0201	44.57	45.28	45.05
J1626.6-7639	246.6553	-76.6502	IBL	0.105	8.92	43.56	0.0065	43.81	43.68	43.43
J1627.3+3148	246.8347	31.814	HBL	0.58	8.41	44.47	0.00369	44.38	45.12	44.99
J1637.6+4548	249.4137	45.8108	HBL	0.192	8.52	43.53	0.019	44.18	44.30	43.47
J1644.2+4546	251.0556	45.776	HBL	0.225	8.97	43.70	0.184	44.58	44.55	43.46
J1647.5+2911	251.8835	29.1837	HBL	0.133	8.77	43.18	0.388	44.51	43.92	43.27
J1647.5+4950	251.8923	49.8336	LBL	0.047	7.98	43.27	0.178	44.05	43.65	43.70
J1653.8+3945	253.4738	39.7595	HBL	0.033	9.91	43.30	1.56	44.27	44.01	43.90
J1658.4+6150	254.62	61.8483	HBL	0.374	7.66	44.15	0.0384	44.54	44.93	44.60
J1704.2+1234	256.0599	12.5752	LBL	0.452	9.45	44.60	0.03	44.59	45.20	45.74
J1730.8+3715	262.7026	37.2641	HBL	0.204	9.71	43.62	0.0631	44.39	44.32	44.06
J1744.0+1935	266.008	19.5956	HBL	0.084	9.69	43.28	0.551	44.41	44.17	43.53
J1745.6+3950	266.4158	39.8412	HBL	0.267	9.52	43.90	0.636	44.84	44.51	43.91
J1751.5+0938	267.8776	9.6456	LBL	0.322	7.98	44.08	0.623	44.91	45.91	45.87
J1754.5-6425	268.639	-64.418	LBL	1.255	8.13	44.91	0.177	45.40	47.17	47.48
J1800.6+7828	270.173	78.4674	LBL	0.691	8.94	45.68	2.22	45.44	46.96	46.93
J1806.8+6949	271.7108	69.827	LBL	0.05	7.10	43.41	1.89	44.43	44.23	43.73
J1853.8+6714	283.4625	67.2487	HBL	0.212	8.96	43.56	0.011	44.13	44.46	43.58
J1911.4-1908	287.8681	-19.1494	HBL	0.138	9.27	43.46	0.44	44.54	44.23	43.94
J1917.7-1921	289.4384	-19.3628	HBL	0.137	9.08	43.82	0.482	44.55	44.69	44.46
J1942.8-3512	295.7173	-35.2012	IBL	0.05	9.01	42.52	0.154	44.05	42.85	42.96

Table 1 – continued .

4FGL name (1)	RA (2)	DEC (3)	Type (4)	Redshift (5)	log M (6)	log L_{disk} (7)	f_{ν} (8)	log P_{kin} (9)	log L_{sy} (10)	log L_{ic} (11)
J1954.6-1122	298.6693	-11.3815	LBL	0.683	8.05	44.46	0.367	45.16	46.16	46.74
J2000.0+6508	300.011	65.1479	HBL	0.047	9.07	42.89	0.25	44.10	44.50	43.89
J2014.3-0047	303.599	-0.7922	HBL	0.23	9.18	44.31	0.125	44.53	44.73	44.34
J2032.0+1219	308.004	12.3279	LBL	1.211	8.31	44.94	0.999	45.64	47.29	47.51
J2049.7-0036	312.4456	-0.616	HBL	0.257	8.00	43.66	0.0058	44.11	44.71	43.78
J2054.8+0015	313.7246	0.257	HBL	0.151	8.75	43.40	0.057	44.26	44.19	43.77
J2108.7-0250	317.1788	-2.8449	HBL	0.149	10.10	43.67	0.127	44.38	44.29	43.62
J2115.9-0113	318.9959	-1.2306	HBL	0.305	8.22	44.21	0.069	44.55	44.80	44.53
J2130.2-7320	322.5524	-73.3348	HBL	0.057	9.49	43.00	0.182	44.12	43.26	42.05
J2134.2-0154	323.5699	-1.9042	LBL	1.283	8.75	44.83	1.69	45.75	47.54	47.56
J2150.8+1118	327.7033	11.3149	HBL	0.495	7.24	44.55	0.0099	44.46	45.40	44.94
J2152.5+1737	328.137	17.6173	LBL	0.872	8.61	44.41	0.681	45.38	46.84	46.66
J2153.1-0041	328.2823	-0.6927	HBL	0.342	9.75	44.16	0.0247	44.44	45.31	44.64
J2158.8-3013	329.7141	-30.2251	HBL	0.116	8.91	43.51	0.49	44.50	45.86	45.35
J2202.7+4216	330.6946	42.2821	LBL	0.069	7.81	43.34	6.05	44.71	45.01	44.69
J2202.7-5637	330.6995	-56.6318	HBL	0.049	9.44	42.66	0.0584	43.90	42.91	41.94
J2204.3+0438	331.0832	4.6401	IBL	0.027	7.32	42.75	0.467	44.02	42.87	42.78
J2206.8-0032	331.7087	-0.5461	LBL	1.053	8.58	44.64	0.152	45.26	46.86	46.93
J2209.7-0451	332.4382	-4.8597	HBL	0.397	8.59	44.45	0.0248	44.50	45.08	44.57
J2211.0-0003	332.7625	-0.0635	HBL	0.362	8.55	44.26	0.0255	44.47	45.14	44.37
J2216.9+2421	334.238	24.3575	LBL	1.033	8.44	45.04	0.528	45.44	47.18	47.09
J2220.5+2813	335.1419	28.2322	HBL	0.149	8.62	43.31	0.0488	44.23	44.12	43.51
J2232.8+1334	338.2245	13.5764	HBL	0.214	8.32	43.55	0.0251	44.26	44.98	43.75
J2243.4-2544	340.8654	-25.7363	LBL	0.774	8.47	44.51	1.1	45.39	46.63	46.57
J2250.0+3825	342.5142	38.4247	HBL	0.119	9.44	43.31	0.104	44.27	44.56	44.13
J2252.6+1245	343.1676	12.7543	HBL	0.497	8.08	44.65	0.0463	44.69	45.25	44.63
J2253.7+1405	343.4483	14.091	HBL	0.327	8.49	44.08	0.0116	44.31	44.98	44.30
J2257.5+0748	344.3874	7.8014	LBL	0.19	9.66	43.75	0.394	44.64	44.63	43.99
J2314.0+1445	348.5081	14.7532	HBL	0.164	9.11	43.55	0.0406	44.24	44.57	44.04
J2315.6-5018	348.914	-50.3127	LBL	0.811	8.41	44.71	0.233	45.18	46.66	46.34
J2319.1-4207	349.7763	-42.1173	HBL	0.055	9.41	43.30	1.67	44.44	43.55	42.57
J2322.7+3436	350.6849	34.6125	HBL	0.098	9.55	42.80	0.0957	44.20	44.09	43.28
J2330.3-2948	352.5806	-29.8072	HBL	0.297	8.99	44.20	0.039	44.45	44.54	44.05
J2343.6+3438	355.9063	34.6403	HBL	0.365	8.47	44.19	0.0349	44.52	45.72	45.16
J2346.7+0705	356.6786	7.0931	HBL	0.172	8.79	43.93	0.303	44.56	44.73	44.02
J2347.0+5141	356.7659	51.6966	HBL	0.044	7.71	42.85	0.251	44.08	43.67	43.51
J2357.4-0152	359.3674	-1.8703	LBL	0.816	7.33	43.91	0.234	45.18	45.91	46.12
J2358.3+3830	359.5883	38.5097	IBL	0.2	7.39	43.27	0.0579	44.36	44.30	44.31

Columns (1) is the 4FGL name of sources; Columns (2) is the Right ascension in decimal degrees; Columns (3) is Declination in decimal degrees; Columns (4) is the Class of sources, low-frequency peaked BL Lac objects (LBL), intermediate objects (IBL), and high-frequency peaked BL Lac objects (HBL); Columns (5) is redshift; Columns (6) is the black hole mass; Columns (7) is the disk luminosity in units erg s^{-1} ; Columns (8) is the 1.4 GHz radio flux in units Jy ; Columns (9) is the jet kinetic power in units erg s^{-1} ; Columns (10) is the synchrotron peak frequency luminosity in units erg s^{-1} ; Columns (11) is the inverse Compton luminosity in units erg s^{-1} . The redshift, black hole mass, accretion disk luminosity, synchrotron peak frequency luminosity and the inverse Compton luminosity comes from the work of [Paliya et al. \(2021\)](#). The 1.4 GHz radio flux comes from the FIRST Survey Catalog: 14Dec17 Version ^a.

^a <http://sundog.stsci.edu/first/catalogs/readme.html>

field to the unamplified magnetic field strength derived from the self-similar ADAF solution as $B_{\phi} = gB$, and $\Omega = \Omega' + \omega$. The H is the vertical half-thickness of the disk. In the case of an ADAF, $H \sim R$ ([Nemmen et al. 2007](#)). Following the method of [Nemmen et al. \(2007\)](#), all physical quantities are estimated at $R = R_{\text{ms}}$ (see APPENDIX A).

4 RESULTS AND DISCUSSION

4.1 Redshift and black hole masses

To better evaluate our results and put them into a context, we studied the distributions of the Fermi BL Lacs of our sample in terms of redshift, black hole mass, jet kinetic power, and accretion disk luminosity. The redshift distribution of Fermi LBL extends to larger values than IBL and HBL (Fig. 1). The average values of redshift are $z = 0.64$ for LBL, $z = 0.26$ for IBL, and $z = 0.25$ for HBL. The range of black hole mass is from $10^{6.5}$ to $10^{10} M_{\odot}$. The average values of black hole mass are $\log M_{\text{BH}} = 8.39$ for LBL, $\log M_{\text{BH}} = 8.34$ for

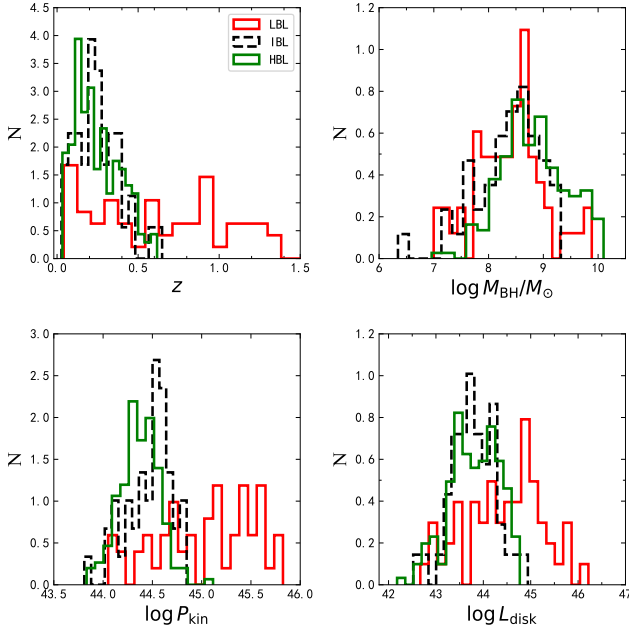


Figure 1. Distribution of the redshifts, black hole mass, jet kinetic power and accretion disk luminosity for the Fermi BL Lacs of our sample. The red line is LBL. The black dashed line is IBL. The green line is HBL.

IBL, and $\log M_{\text{BH}} = 8.82$ for HBL. Cha et al. (2014) also found that FSRQs and LBL tend to have higher redshift and gamma-ray luminosity than HBL. They suggested that the evolutionary track of Fermi blazars is FSRQs→LBL→HBL.

4.2 Jet kinetic power and accretion disk luminosity

The range of jet kinetic power is mainly from $10^{44.0}$ to $10^{46.0}$ erg s $^{-1}$. The LBL tends to have higher jet kinetic power than IBL and HBL (Fig. 1). The average values of jet kinetic power are $\log P_{\text{kin}} = 45.04$ for LBL, $\log P_{\text{kin}} = 44.26$ for IBL, and $\log P_{\text{kin}} = 44.37$ for HBL. The scope of accretion disk luminosity is mainly from $10^{42.0}$ to $10^{46.0}$ erg s $^{-1}$. The LBL also tends to have higher accretion disk luminosity than IBL and HBL. The average values of accretion disk luminosity are $\log L_{\text{disk}} = 44.45$ for LBL, $\log L_{\text{disk}} = 43.79$ for IBL, and $\log L_{\text{disk}} = 43.80$ for HBL. Chen et al. (2015a) found that the LBL tends to have higher jet kinetic power and BLR luminosity than HBL and IBL using a smaller sample than the one we consider here (see Figure 7 of Chen et al. (2015a)). Our results are consistent with theirs.

4.3 Accretion rates

Paliya et al. (2021) suggested that the physical properties of Fermi blazars are likely to be controlled by the accretion rate in Eddington units. Therefore, we study the accretion rate distribution of Fermi BL Lacs. Using the relative contribution of individual lines to the total BLR luminosity (see Section 2.2), we obtain the total line luminosity L_{lines} . Wang et al. (2002) defined a "line accretion rate" and its dimensionless form as follows

$$\lambda = \frac{L_{\text{lines}}}{L_{\text{Edd}}}, L_{\text{lines}} = \xi L_{\text{disk}}. \quad (7)$$

Assuming that most of the line luminosity (L_{lines}) is photoionized by the accretion disk (Netzer 1990), the L_{lines} should be proportional to the total luminosity of the accretion disks. Netzer (1990) defined $\xi \approx 0.1$. The L_{Edd} is Eddington luminosity, $L_{\text{Edd}} = 1.3 \times 10^{38} (M_{\text{BH}}/M_{\odot}) \text{ erg s}^{-1}$. Wang et al. (2002) got the relation between λ and the dimensionless accretion rate (\dot{m}) for an optically thin ADAFs as follows

$$\dot{m} = 2.17 \times 10^{-2} \alpha_{0.3} \xi_{-1}^{-1/2} \lambda_{-4}^{1/2}, \quad (8)$$

where $\alpha_{0.3} = \alpha/0.3$, $\xi_{-1} = \xi/0.1$, and $\lambda_{-4} = \lambda/10^{-4}$ (Wang et al. 2003). The viscosity parameters α is 0.3 (Narayan & Yi 1995). Narayan et al. (1998) suggested that an optical thin ADAFs appears when $\dot{m} \leq \alpha^2$. Equation (8) can then be rewritten as

$$\lambda_1 = 1.72 \times 10^{-3} \xi_{-1} \alpha_{0.3}^2. \quad (9)$$

Optically thin ADAFs require $\lambda < \lambda_1$. The optically thick, geometrically thin disk (SS) obey (Wang et al. 2003)

$$\dot{m} = 10 \xi_{-1}^{-1} \lambda, \quad (10)$$

and the condition $1 > \dot{m} \geq \alpha^2$ gives

$$\lambda_2 = 9.0 \times 10^{-3} \xi_{-1} \alpha_{0.3}^2. \quad (11)$$

A standard thin disk satisfies $\lambda \geq \lambda_2$ (Wang et al. 2003). When the accretion rate reaches $\dot{m} \geq 1$, we have

$$\lambda_3 = 0.1 \xi_{-1}. \quad (12)$$

A slim disk requires $\lambda \geq \lambda_3$ (Wang et al. 2002, 2003), namely Super-Eddington accretion (SEA). It is worth noting that in the transition region between λ_1 and λ_2 , the accretion flow may be in a hybrid state, in which the standard disk coexists with ADAFs. Some authors have shown that hybrid states are possible in the accretion disk of AGN (e.g., Quataert et al. 1999; Różańska & Czerny 2000; Ho et al. 2000). Gu & Lu (2000) suggested that the conversion of a SS disk to an ADAFs is possible through evaporation (Liu et al. 1999). The transition radius depends on accretion rate, black hole mass, and viscosity. However, in such a regime, the disk structure is complex.

Figure 2 shows that the three critical values of λ define four regimes in accretion states. The average values of λ for LBL, IBL and HBL are $\langle \log \lambda \rangle|_{\text{LBL}} = -3.05$, $\langle \log \lambda \rangle|_{\text{IBL}} = -3.67$ and $\langle \log \lambda \rangle|_{\text{HBL}} = -4.14$, respectively. We find that the LBL has higher accretion rates than IBL and HBL, which could explain why LBL have more luminous disks and more powerful jets than HBL (see Fig. 1). Wang et al. (2002) also found that the HBL has lower accretion rates than LBL. We investigated the differences in the distribution of accretion rates using the parameter T-test, nonparametric Kolmogorov Smirnov (K-S) test, and Kruskal Wallis H test. The parameter T-test is mainly used to test whether there is a difference in the mean accretion rate between two independent samples. The nonparametric K-S test and Kruskal Wallis H test are mainly used to test whether there are differences in the distribution of accretion rates between two independent samples. We assume that there are differences in the three tests at the same time, so there is a significant difference in the accretion rate between the two samples. According to the parameter T-test ($P = 1.11 \times 10^{-15}$, significant probability $P < 0.05$), nonparametric K-S test ($P = 1.01 \times 10^{-15}$, significant probability $P < 0.05$), and Kruskal-Wallis H-test ($P = 1.99 \times 10^{-14}$, significant probability $P < 0.05$), we find

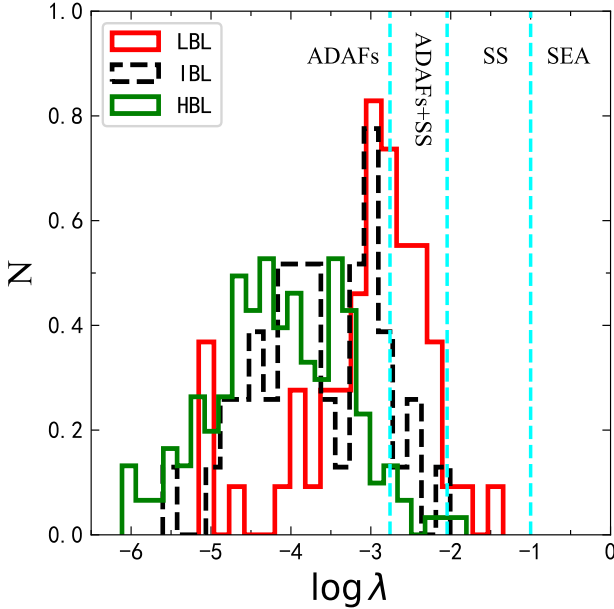


Figure 2. The distribution of λ for the Fermi BL Lacs of our sample. Line styles identify a different class of BL Lacs as in Fig. 1. The cyan dashed lines are λ_1 , λ_2 , and λ_3 , respectively. The distribution of λ is divided into four regions, corresponding to different states of the accretion disks:(1) $\lambda < \lambda_1$ (pure ADAFs); (2) $\lambda_1 \leq \lambda \leq \lambda_2$ (ADAFs+SS); (3) $\lambda_2 \leq \lambda \leq \lambda_3$ (SS); (4) $\lambda \geq \lambda_3$ (SEA).

that the distributions of accretion rates between LBL and HBL are significantly different. The parameter T-test shows that there is a significant difference of the distributions of accretion rates between IBL and LBL ($P = 0.0002$). Through a nonparametric K-S test ($P = 0.0006$) and a Kruskal–Wallis H-test ($P = 9.38 \times 10^{-5}$), we find that the distributions of accretion rates between IBL and LBL are significantly different. Through a parameter T-test ($P = 0.0008$), nonparametric K-S test ($P = 0.006$), and Kruskal–Wallis H-test ($P = 0.0008$), we find that the distributions of accretion rates between IBL and HBL are significantly different.

From Figure 2, we find that about 62% HBL and 14% IBL have pure optically thin ADAFs, while about 7% LBL have ADAFs+SS. Cao (2002) found that the accretion flows in all HBL are in the ADAF state. Wang et al. (2003) also found that the low-power HBLs and LBLs have pure optically thin ADAFs. However, the LBLs also may have a hybrid structure consisting of an SS disk plus optically thin ADAFs. Cao (2003) also found that the BL Lacs have different accretion modes. They proposed that the BL Lacs have ADAFs in the inner region of the disk, and it becomes a standard thin disk in the outer region, i.e., ADAFs+SS scenario.

4.4 Relation between jet kinetic power and black hole mass

Because our sample has an accretion rate compatible with an ADAFs regime (Fig 2), we considered the jet power of the BZ mechanism and the jet power of the hybrid model in the ADAFs scenario. The relation between the jet power extracted from the ADAFs for the BZ and hybrid models and the black hole mass is shown in Figure 3. In order to estimate the maximum jet power of BZ model and Hybrid model, we use accretion rates $\dot{m} = 0.01$, and the disk viscosity parameter $\alpha = 0.3$ (Narayan & Yi 1995). The spin of black hole $j = 0.98$ is adopted. The black dashed line is the BZ jet model, and

the black solid line is the Hybrid jet model. The red dot is LBL. The black dot is the IBL. The green triangle is HBL. The cyan circle is sources with ADAFs+SS. We find that about 7% LBL, 9% IBL, and 32% HBL are below the maximal BZ jet power expected to be extracted from ADAFs (Fig.3, dashed line). These results show that the jet kinetic power of LBL and IBL can hardly be explained by the BZ jet model. However, about 26% LBLs, 72% IBLs, and 94% HBLs are below the solid line when we consider the hybrid model. These results show that most of the IBL and HBL can be explained by the Hybrid jet model. Most LBLs cannot be explained by the BZ jet model or Hybrid jet model. These sources with ADAFs+SS have high jet power, which makes them unable to be explained by BZ or hybrid models. There are two possible explanations for the jet power of the LBL. One is that these LBLs require other jet models, such as an accretion disk with magnetization-driven outflows (Cao & Spruit 2013; Li 2014; Cao 2016, 2018; Li & Cao 2022). Cao & Spruit (2013) proposed that if the most angular momentum of the gas in the thin disk is taken away by the magnetically driven outflows, the radial velocity of the disk will increase significantly, so the external field can be significantly enhanced in the inner region of the thin disk with the magnetically driven outflows (Li & Cao 2019; Cao 2018). Thereby, the expected jet kinetic power is higher than in the case of the BZ or hybrid model, as we observed in the data. The other is that the LBL has a strong beaming effect. Lister et al. (2011) found that the LBL has generally higher Doppler factors than HBL, which implies that the LBL has a strong beaming effect. Because of the beaming effect, the jet kinetic power could be overestimated. The "real" jet power, in this scenario, may be lower and compatible with models.

It is widely believed that large-scale magnetic fields play a crucial role in the acceleration and collimation of jets and/or outflows (e.g., Pudritz et al. 2007). The origin of the large-scale magnetic field passing through the accretion disk has not been well understood. Some studies suggest that large-scale magnetic fields that accelerate jets or outflows may be formed by weak external field advection (e.g., Bisnovatyi-Kogan & Blinnikov 1977; Bisnovatyi-Kogan & Ruzmaikin 1976; Spruit & Uzdensky 2005). However, Lubow et al. (1994) found that in the geometrically thin accretion disk ($H/R \leq 1$), the advection in the external field is quite ineffective because of its small radial velocity. This may imply that the field in the inner region of the disk is not much stronger than the external weak field, which cannot accelerate strong jets in radio-loud quasars (Lubow et al. 1994). A few mechanisms were suggested to alleviate the difficulty of field advection in the thin disk (e.g., Spruit & Uzdensky 2005). Some people believe that the hot corona above the disk can effectively drag the external field inward, that is, the so-called "coronal mechanism" (see Beckwith et al. 2009). The radial velocity of the gas above the disk can be greater than the radial velocity of the mid-plane of the disk, which partly solves the problem of inefficient field advection in the thin disk (Lovelace et al. 2009; Guilet & Ogilvie 2012, 2013). Recently, Cao (2018) suggested that powerful jets can be accelerated by the coronal magnetic field. Cao (2004) found that the jets are accelerated from the disk coronas for radio-loud quasars. Zhu et al. (2020) found a close connection between corona-disk-jet for radio-loud quasars. At the same time, some authors found that FSRQs and LBL have similar spectral properties, such as particle acceleration mechanism (e.g., Chen et al. 2021). These results indicate that the jet kinetic power of LBL may also be explained by the coronal magnetic field.

Chen et al. (2023b) found that the jet kinetic power of jetted AGNs are powered by the BZ mechanism based on the relation between jet kinetic power and accretion disk luminosity. Our results are slightly

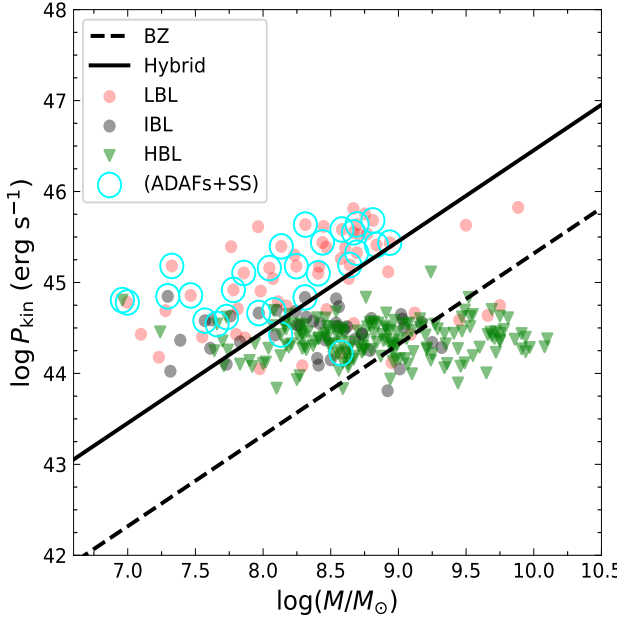


Figure 3. The jet kinetic power versus the black hole mass for the Fermi BL Lacs of our sample. The black dashed line is the maximum jet power expected in the case of BZ jet formation mechanism. The black solid line is the maximum jet power expected in the case of Hybrid jet formation mechanism. The red dot is LBL. The black dot is IBL. The green triangle is HBL. The cyan circle is sources with ADAFs+SS.

different from those of Chen et al. (2023b). The main reason is that we calculate the maximum jet power of the BZ mechanism and the hybrid model based on the theory, and then compare the maximum jet power of the BZ mechanism and the hybrid model with the observed jet kinetic power. The work of Chen et al. (2023b) is mainly based on whether the slope of the relationship between jet kinetic power and accretion disk luminosity is 1 to judge whether their jet kinetic power is dominated by the BZ mechanism. In the work of Chen et al. (2023b), it is assumed that the jet kinetic power of jetted AGN is dominated by Poynting flux, and then it is obtained that the slope of the relationship between the maximum jet power of BZ mechanism and the luminosity of accretion disk is equal to 1 (Ghisellini 2006). Finally, the slope of the relationship between jet kinetic power and accretion disk luminosity is compared with theory to further judge whether the jet of jetted AGN is dominated by BZ mechanism. However, some studies have found that the jet power of jetted AGN is not dominated by the Poynting flux (e.g., McKinney et al. 2012; Zdziarski et al. 2015; Paliya et al. 2017; Chen et al. 2023a).

In Figure 4, we show the results as in Fig 3, but the dashed lines are $P_{\text{jet}}/L_{\text{Edd}} = 0.01, 0.1, 1$, respectively. The jet kinetic power of all Fermi BLLacs is less than $1L_{\text{Edd}}$. We find that about 79% LBL is located in $\sim 0.01 - 1L_{\text{Edd}}$. As a comparison, the jet power expected in case of coronal mechanism is at most 0.05 Eddington (Cao 2018). Cao & Spruit (2013) suggested that most of the angular momentum of the accretion disk is excluded from magnetization-driven outflows, and the magnetic field will be enhanced compared with the thin disk without outflow. The magnetic field dragged inward by the accretion disc with magnetization-driven outflows may accelerate the jet in source with high jet power. The jet kinetic power of these LBLs may be explained by the magnetization-driven outflows model (Cao 2018).

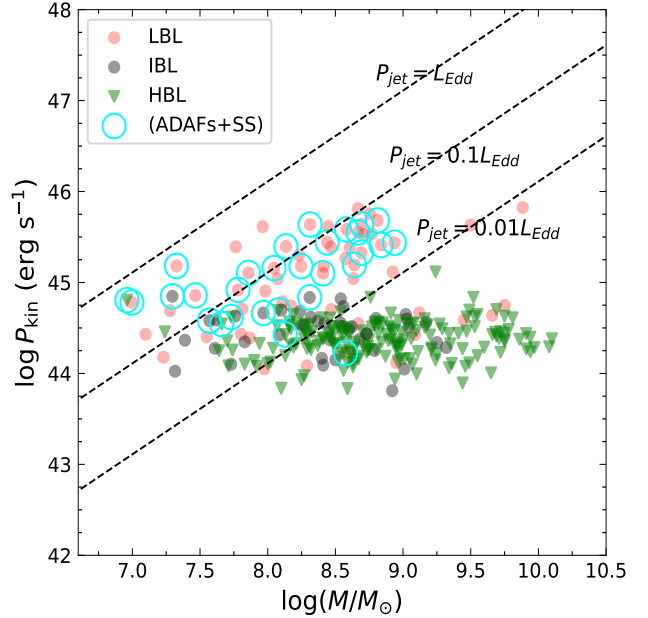


Figure 4. The jet kinetic power versus the black hole mass. The dashed lines are $P_{\text{jet}}/L_{\text{Edd}} = 0.01, 0.1, 1$, respectively. The different symbols are as in Fig.3.

We also find that the jet kinetic power of LBL depends on the mass of the black hole, while the jet kinetic power of HBL does not seem to depend on the mass of the black hole. Ghosh & Abramowicz (1997) found that it is possible for the standard disks to find two regimes, which may be radiation pressure dominated (RPD) or gas pressure dominated (GPD). The jet kinetic power depends on the mass of the black hole, indicating that the accretion disk is dominated by radiation pressure. The jet kinetic power depends on the accretion ($L_{\text{bol}}/L_{\text{Edd}}$), indicating that the accretion disk is dominated by gas pressure (Ghosh & Abramowicz 1997; Foschini 2011; Chen et al. 2015a). Our results imply that the accretion disk of LBL may be dominated by radiation pressure, while that of HBL is not dominated by radiation pressure. The accretion disks of HBL may be dominated by gas pressure. In the future, when our source has the bolometric luminosity, we will test these results. Chen et al. (2015a) also found that the accretion disks of FSRQs and LBL are dominated by radiation pressure, while the accretion disks of HBL and IBL seem to be dominated by gas pressure.

4.5 Relation between jet kinetic power and accretion disk luminosity

There is evidence that there is a positive correlation between jet power and accretion luminosity in jetted AGN (e.g., Rawlings & Saunders 1991; Wang et al. 2004; Gu et al. 2009; Ghisellini et al. 2010; Sbarro et al. 2014; Ghisellini et al. 2014; Paliya et al. 2019). The relation between jet kinetic power and accretion disk luminosity is shown in Figure 5. We find a significant correlation between jet kinetic power and accretion disk luminosity for the whole sample ($r = 0.74, P = 5.10 \times 10^{-50}$). The tests of Spearman ($r = 0.69, P = 1.58 \times 10^{-41}$) and Kendall tau ($r = 0.52, P = 3.81 \times 10^{-37}$) also show a significant correlation between jet kinetic power and accretion disk luminosity for the whole sample. The best fitting equation given by least square linear regression is $\log P_{\text{kin}} = (0.46 \pm 0.03) \log L_{\text{disk}} + (24.39 \pm 1.09)$. At the same time, we also find that the sources with ADAFs+SS fol-

low the same relation. However, [Rajguru & Chatterjee \(2022\)](#) suggested that the correlations are often driven by the common redshift dependence. They found a weak correlation between jet power and accretion disk luminosity when the redshift was excluded. We test their results. Partial correlation shows a moderately weak correlation between jet kinetic power and accretion disk luminosity when redshift dependence is excluded for the whole sample ($r = 0.12, P = 0.03$). We use Pearson correlation analysis for other types of AGNs. There is **also** a significant correlation between jet kinetic power and accretion disk luminosity for the LBL ($r = 0.81, P = 3.51 \times 10^{-14}$). The best fitting equation given by least square linear regression for the LBL is $\log P_{\text{kin}} = (0.48 \pm 0.05) \log L_{\text{disk}} + (23.46 \pm 2.13)$. Partial correlation shows a moderately weak correlation between jet kinetic power and accretion disk luminosity when redshift dependence is excluded for the LBL ($r = 0.34, P = 0.009$). There is a significant correlation between jet kinetic power and accretion disk luminosity for the IBL+HBL ($r = 0.60, P = 3.09 \times 10^{-23}$). The best fitting equation given by least square linear regression for the IBL+HBL is $\log P_{\text{kin}} = (0.25 \pm 0.02) \log L_{\text{disk}} + (33.42 \pm 0.98)$. Partial correlation shows a moderately weak correlation between jet kinetic power and accretion disk luminosity when redshift dependence is excluded for the IBL+HBL ($r = 0.24, P = 0.003$). We find that the slope of the relation between jet kinetic power and accretion disk luminosity for the LBL is slightly different from that of IBL+HBL, and the slope of LBL is greater than that of IBL+HBL. [Paliya et al. \(2017\)](#) found that the slope of the relation between jet power and accretion disk luminosity is 0.46 using both 324 γ -ray detected and 191 γ -ray undetected blazars. [Chen et al. \(2023a\)](#) also found that the slope of the relation between jet kinetic power and accretion disk luminosity is 0.51 ± 0.18 using 38 gamma-ray-emitting radio galaxies. Our results are similar to the results of [Paliya et al. \(2017\)](#) and [Chen et al. \(2023a\)](#). [Ghisellini et al. \(2014\)](#) found that the slope of the relation between jet power and accretion disk luminosity is 0.92 using 217 γ -ray detected blazars. [Chen et al. \(2023b\)](#) found that the slope of the relation between jet kinetic power and accretion disk luminosity is 1.00 ± 0.02 for the whole sample (FSRQs+BL Lacs+gamma-ray-emitting narrow-line Seyfert 1 galaxies), 0.83 ± 0.04 for FSRQs, 1.00 ± 0.05 for BL Lacs, 0.73 ± 0.15 for gamma-ray-emitting narrow-line Seyfert 1 galaxies. Because we mainly use the jet kinetic power to replace the total jet power. Therefore, we also examined all relationships including 10% of jet kinetic power and found that all relationships were valid in our work.

4.6 Relation between IC Luminosity versus Synchrotron Luminosity

Figure 6 shows a relation between IC luminosity and synchrotron luminosity for Fermi BL Lacs. We find a significant correlation between IC luminosity and synchrotron luminosity for the whole sample ($r = 0.95, P = 2.06 \times 10^{-143}$). The tests of Spearman ($r = 0.92, P = 7.66 \times 10^{-113}$) and Kendall tau ($r = 0.76, P = 3.47 \times 10^{-80}$) also show a significant correlation between IC luminosity and synchrotron luminosity for the whole sample. The best fitting equation given by least square linear regression is $\log L_{\text{IC}} = (1.16 \pm 0.02) \log L_{\text{syn}} + (-7.58 \pm 1.00)$. We find that the slope of the relation between IC luminosity and synchrotron luminosity is close to 1.0. According to [Ghisellini \(1996\)](#) ($L_{\text{EC}} \sim L_{\text{syn}}^{1.5}$, $L_{\text{SSC}} \sim L_{\text{syn}}^{1.0}$), our results suggest that the IC component of Fermi BL Lacs is dominated by the SSC process. Some authors have confirmed this conclusion (e.g., [Celotti & Ghisellini 2008](#); [Ghisellini et al. 2010](#); [Lister et al. 2011](#); [Ackermann et al. 2012](#); [Wu et al. 2014](#);

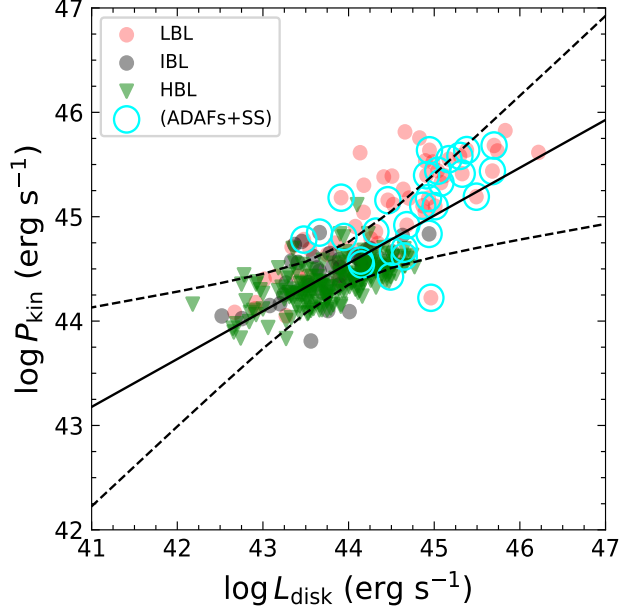


Figure 5. Relation between jet kinetic power and accretion disk luminosity for the Fermi BL Lacs of our sample. The different symbols are as in Fig.3. The solid line corresponds to the best-fitting linear models. The dashed lines indicate 3σ confidence bands of the best fits, namely it refers to the significance level $\alpha = 0.01$, with a 99% probability that the measured results are within this range.

[Marchesini et al. 2019](#); [La Mura et al. 2022](#)). [Xue et al. \(2016\)](#) found that the slope of the relation between IC luminosity and synchrotron luminosity for 28 Fermi BL Lacs is $k_{\text{BLLacs}} = 1.12 \pm 0.10$. Our work confirms the results of previous studies.

5 SUMMARY

We use a large sample of Fermi BL Lacs to study the physical properties of their jets, and the main conclusions are as follows:

(1) We find that that LBL tends to have higher accretion disk luminosity and jet kinetic power than HBL, which could be due to a higher accretion rate.

(2) We find that LBL has a higher accretion rate than IBL and HBL. Almost all IBL and HBL have pure optically thin ADAFs. However, some LBLs may have a hybrid structure consisting of an SS disk plus optically thin ADAFs.

(3) We study the jet power of the BZ mechanism and the hybrid mechanism based on the self-similar solution of the ADAFs around the Kerr black hole. Through the relationship between jet power and black hole mass, we find that the jet kinetic power of about 72% IBL and 94% HBL can be explained by the hybrid model. However, only 7% LBL can be explained by the BZ model, and only 26% LBL can be explained by the hybrid model.

(4) The jet kinetic power of about 79% LBL is located at $\sim 0.01 - 1 L_{\text{Edd}}$. The jet kinetic power of these sources may be interpreted by magnetization-driven outflows.

(5) There is a significant correlation between jet kinetic power and accretion disk luminosity for Fermi BL Lacs. However, this correlation becomes weak when excluding the dependence of redshift.

(6) We find a significant correlation between IC luminosity and synchrotron luminosity for Fermi BL Lacs. The slope of the relation

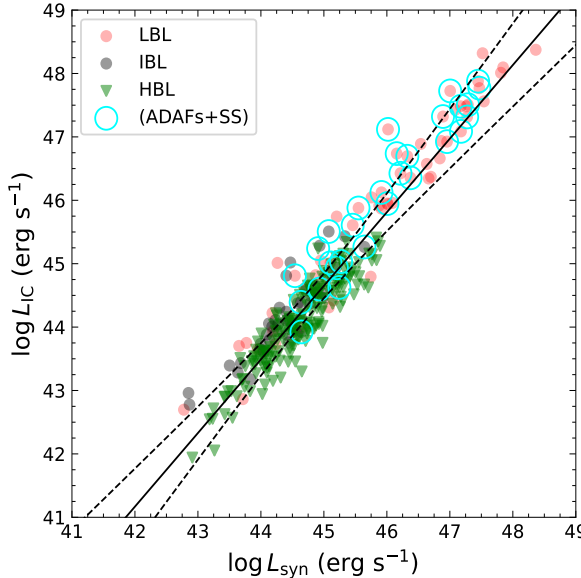


Figure 6. The inverse Compton luminosity versus synchrotron luminosity for the Fermi BL Lacs of our sample. The different symbols are as in Fig.3. The solid and dashed lines describe the best fit linear model and its uncertainty as in Fig. 5.

between IC luminosity and synchrotron luminosity in Fermi BL Lacs is 1.16 ± 0.02 , which implies that the high-energy components of Fermi BL Lacs are dominated by the SSC process.

ACKNOWLEDGEMENTS

We are very grateful to the referee and Editor for the very helpful report. Yongyun Chen is grateful for financial support from the National Natural Science Foundation of China (No. 12203028). This work was support from the research project of Qijing Normal University (2105098001/094). This work is supported by the youth project of Yunnan Provincial Science and Technology Department (202101AU070146, 2103010006). Yongyun Chen is grateful for funding for the training Program for talents in Xingdian, Yunnan Province. QSGU is supported by the National Natural Science Foundation of China (No. 12192222, 12192220 and 12121003). We also acknowledge the science research grants from the China Manned Space Project with NO. CMS-CSST-2021-A05. This work is supported by the National Natural Science Foundation of China (11733001 and U2031201). D.R.X. acknowledge the science research grants from the China Manned Space Project with No. CMS-CSST- 2021-A06, Yunnan Province Youth Top Talent Project (YNWR-QNBJ-2020-116) and the CAS “Light of West China” Program.

DATA AVAILABILITY

All the data used here are available upon reasonable request. All data are in Table 1.

REFERENCES

- Abdo A. A., et al., 2010, *ApJ*, **716**, 30
- Abdollahi S., et al., 2020, *ApJS*, **247**, 33
- Ackermann M., et al., 2012, *ApJ*, **751**, 159
- Ajello M., et al., 2020, *ApJ*, **892**, 105
- Arbeiter C., Pohl M., Schlickeiser R., 2002, *A&A*, **386**, 415
- Atwood W. B., et al., 2009, *ApJ*, **697**, 1071
- Baldwin J. A., Netzer H., 1978, *ApJ*, **226**, 1
- Bardeen J. M., Press W. H., Teukolsky S. A., 1972, *ApJ*, **178**, 347
- Becker R. H., White R. L., Helfand D. J., 1995, *ApJ*, **450**, 559
- Beckwith K., Hawley J. F., Krolik J. H., 2009, *ApJ*, **707**, 428
- Bîrzan L., McNamara B. R., Nulsen P. E. J., Carilli C. L., Wise M. W., 2008, *ApJ*, **686**, 859
- Bisnovatyi-Kogan G. S., Blinnikov S. I., 1977, *A&A*, **59**, 111
- Bisnovatyi-Kogan G. S., Ruzmaikin A. A., 1976, *Ap&SS*, **42**, 401
- Blandford R. D., Payne D. G., 1982, *MNRAS*, **199**, 883
- Blandford R. D., Rees M. J., 1978, *Phys. Scr.*, **17**, 265
- Blandford R. D., Znajek R. L., 1977, *MNRAS*, **179**, 433
- Błażejowski M., Sikora M., Moderski R., Madejski G. M., 2000, *ApJ*, **545**, 107
- Bloom S. D., Marscher A. P., 1996, *ApJ*, **461**, 657
- Calderone G., Ghisellini G., Colpi M., Dotti M., 2013, *MNRAS*, **431**, 210
- Cao X., 2002, *ApJ*, **570**, L13
- Cao X., 2003, *ApJ*, **599**, 147
- Cao X., 2004, *ApJ*, **613**, 716
- Cao X., 2016, *ApJ*, **833**, 30
- Cao X., 2018, *MNRAS*, **473**, 4268
- Cao X., Jiang D. R., 1999, *MNRAS*, **307**, 802
- Cao X., Spruit H. C., 2013, *ApJ*, **765**, 149
- Cavagnolo K. W., McNamara B. R., Nulsen P. E. J., Carilli C. L., Jones C., Bîrzan L., 2010, *ApJ*, **720**, 1066
- Cavaliere A., D’Elia V., 2002, *ApJ*, **571**, 226
- Celotti A., Ghisellini G., 2008, *MNRAS*, **385**, 283
- Celotti A., Padovani P., Ghisellini G., 1997, *MNRAS*, **286**, 415
- Cha Y., Zhang H., Zhang X., Xiong D., Li B., Dong X., Li J., 2014, *Ap&SS*, **349**, 895
- Chen Y.-Y., Zhang X., Xiong D., Yu X., 2015a, *AJ*, **150**, 8
- Chen Y. Y., Zhang X., Zhang H. J., Yu X. L., 2015b, *MNRAS*, **451**, 4193
- Chen Y., et al., 2021, *ApJ*, **906**, 108
- Chen Y., Gu Q., Fan J., Yu X., Ding N., Xiong D., Guo X., 2023a, *ApJS*, **265**, 60
- Chen Y., Gu Q., Fan J., Yu X., Ding N., Guo X., Xiong D., 2023b, *MNRAS*, **519**, 6199
- Churazov E., Brüggen M., Kaiser C. R., Böhringer H., Forman W., 2001, *ApJ*, **554**, 261
- Deng X.-C., Hu W., Lu F.-W., Dai B.-Z., 2021, *MNRAS*, **504**, 878
- Dermer C. D., Schlickeiser R., 1993, *ApJ*, **416**, 458
- Dermer C. D., Schlickeiser R., Mastichiadis A., 1992, *A&A*, **256**, L27
- Dermer C. D., Sturner S. J., Schlickeiser R., 1997, *ApJS*, **109**, 103
- Esin A. A., McClintock J. E., Narayan R., 1997, *ApJ*, **489**, 865
- Fabian A. C., et al., 2000, *MNRAS*, **318**, L65
- Foschini L., 2011, *Research in Astronomy and Astrophysics*, **11**, 1266
- Foschini L., et al., 2022, *Universe*, **8**, 587
- Francis P. J., Hewett P. C., Foltz C. B., Chaffee F. H., Weymann R. J., Morris S. L., 1991, *ApJ*, **373**, 465
- Garofalo D., Evans D. A., Sambruna R. M., 2010, *MNRAS*, **406**, 975
- Ghisellini G., 1996, in Ekers R. D., Fanti C., Padrielli L., eds, Vol. 175, *Extragalactic Radio Sources*. p. 413
- Ghisellini G., 2006, in VI Microquasar Workshop: Microquasars and Beyond. p. 27.1 ([arXiv:astro-ph/0611077](https://arxiv.org/abs/astro-ph/0611077)), doi:10.22323/1.033.0027
- Ghisellini G., et al., 1997, *A&A*, **327**, 61
- Ghisellini G., Tavecchio F., Ghirlanda G., 2009, *MNRAS*, **399**, 2041
- Ghisellini G., Tavecchio F., Foschini L., Ghirlanda G., Maraschi L., Celotti A., 2010, *MNRAS*, **402**, 497
- Ghisellini G., Tavecchio F., Foschini L., Ghirlanda G., 2011, *MNRAS*, **414**, 2674
- Ghisellini G., Tavecchio F., Maraschi L., Celotti A., Sbarato T., 2014, *Nature*, **515**, 376
- Ghosh P., Abramowicz M. A., 1997, *MNRAS*, **292**, 887
- Graham A. W., 2007, *MNRAS*, **379**, 711

- Gu W.-M., Lu J.-F., 2000, *ApJ*, **540**, L33
 Gu M., Cao X., Jiang D. R., 2009, *MNRAS*, **396**, 984
 Guilet J., Ogilvie G. I., 2012, *MNRAS*, **424**, 2097
 Guilet J., Ogilvie G. I., 2013, *MNRAS*, **430**, 822
 Gürtekin K., et al., 2009, *ApJ*, **698**, 198
 Hawley J. F., Gammie C. F., Balbus S. A., 1995, *ApJ*, **440**, 742
 Ho L. C., Rudnick G., Rix H.-W., Shields J. C., McIntosh D. H., Filippenko A. V., Sargent W. L. W., Eracleous M., 2000, *ApJ*, **541**, 120
 Jones T. W., O'Dell S. L., Stein W. A., 1974, *ApJ*, **188**, 353
 Kauffmann G., Haehnelt M., 2000, *MNRAS*, **311**, 576
 Komossa S., Xu D. W., Wagner A. Y., 2018, *MNRAS*, **477**, 5115
 Kormendy J., Richstone D., 1995, *ARA&A*, **33**, 581
 La Mura G., Becerra Gonzalez J., Chiaro G., Ciroi S., Otero-Santos J., 2022, *MNRAS*, **515**, 4810
 Li S.-L., 2014, *ApJ*, **788**, 71
 Li J., Cao X., 2019, *ApJ*, **872**, 149
 Li J.-W., Cao X., 2022, *ApJ*, **926**, 11
 Li H. Z., Xie G. Z., Yi T. F., Chen L. E., Dai H., 2010, *ApJ*, **709**, 1407
 Lister M. L., et al., 2011, *ApJ*, **742**, 27
 Liu B. F., Yuan W., Meyer F., Meyer-Hofmeister E., Xie G. Z., 1999, *ApJ*, **527**, L17
 Livio M., Ogilvie G. I., Pringle J. E., 1999, *ApJ*, **512**, 100
 Lovelace R. V. E., Rothstein D. M., Bisnovatyi-Kogan G. S., 2009, *ApJ*, **701**, 885
 Lubow S. H., Papaloizou J. C. B., Pringle J. E., 1994, *MNRAS*, **267**, 235
 MacDonald D., Thorne K. S., 1982, *MNRAS*, **198**, 345
 Magorrian J., et al., 1998, *AJ*, **115**, 2285
 Maraschi L., Tavecchio F., 2003, *ApJ*, **593**, 667
 Maraschi L., Ghisellini G., Celotti A., 1992, *ApJ*, **397**, L5
 Marchesini E. J., Paggi A., Massaro F., Masetti N., D'Abrusco R., Andruhov I., de Menezes R., 2019, *A&A*, **631**, A150
 Marscher A. P., Gear W. K., 1985, *ApJ*, **298**, 114
 Massaro E., Perri M., Giommi P., Nesci R., 2004, *A&A*, **413**, 489
 Massaro E., Tramacere A., Perri M., Giommi P., Tosti G., 2006, *A&A*, **448**, 861
 McKinney J. C., Tchekhovskoy A., Blandford R. D., 2012, *MNRAS*, **423**, 3083
 McNamara B. R., et al., 2000, *ApJ*, **534**, L135
 Meier D. L., 1999, *ApJ*, **522**, 753
 Meier D. L., 2001, *ApJ*, **548**, L9
 Meyer E. T., Fossati G., Georganopoulos M., Lister M. L., 2012, *ApJ*, **752**, L4
 Narayan R., Yi I., 1995, *ApJ*, **452**, 710
 Narayan R., Mahadevan R., Quataert E., 1998, in Abramowicz M. A., Björnsen G., Pringle J. E., eds, Theory of Black Hole Accretion Disks. pp 148–182 ([arXiv:astro-ph/9803141](https://arxiv.org/abs/astro-ph/9803141)), doi:10.48550/arXiv.astro-ph/9803141
 Nemmen R. S., Bower R. G., Babul A., Storchi-Bergmann T., 2007, *MNRAS*, **377**, 1652
 Nemmen R. S., Georganopoulos M., Guiriec S., Meyer E. T., Gehrels N., Sambruna R. M., 2012, *Science*, **338**, 1445
 Netzer H., 1990, in Blandford R. D., Netzer H., Woltjer L., Courvoisier T. J. L., Mayor M., eds, Active Galactic Nuclei. pp 57–160
 Padovani P., Giommi P., 1996, *MNRAS*, **279**, 526
 Paliya V. S., Marcotulli L., Ajello M., Joshi M., Sahayanathan S., Rao A. R., Hartmann D., 2017, *ApJ*, **851**, 33
 Paliya V. S., Parker M. L., Jiang J., Fabian A. C., Brenneman L., Ajello M., Hartmann D., 2019, *ApJ*, **872**, 169
 Paliya V. S., Domínguez A., Ajello M., Olmo-García A., Hartmann D., 2021, *ApJS*, **253**, 46
 Pudritz R. E., Ouyed R., Fendt C., Brandenburg A., 2007, in Reipurth B., Jewitt D., Keil K., eds, Protostars and Planets V. p. 277 ([arXiv:astro-ph/0603592](https://arxiv.org/abs/astro-ph/0603592)), doi:10.48550/arXiv.astro-ph/0603592
 Quataert E., Di Matteo T., Narayan R., Ho L. C., 1999, *ApJ*, **525**, L89
 Rajguru G., Chatterjee R., 2022, *Phys. Rev. D*, **106**, 063001
 Rawlings S., Saunders R., 1991, *Nature*, **349**, 138
 Rees M. J., 1967, *MNRAS*, **137**, 429
 Różańska A., Czerny B., 2000, *A&A*, **360**, 1170
 Sbarro T., Ghisellini G., Maraschi L., Colpi M., 2012, *MNRAS*, **421**, 1764
 Sbarro T., Padovani P., Ghisellini G., 2014, *MNRAS*, **445**, 81
 Sikora M., Begelman M. C., Rees M. J., 1994, *ApJ*, **421**, 153
 Silk J., Rees M. J., 1998, *A&A*, **331**, L1
 Spruit H. C., Uzdensky D. A., 2005, *ApJ*, **629**, 960
 Thorne K. S., Price R. H., MacDonald D. A., 1986, Black holes: The membrane paradigm
 Tombesi F., Sambruna R. M., Reeves J. N., Braito V., Ballo L., Gofford J., Cappi M., Mushotzky R. F., 2010, *ApJ*, **719**, 700
 Urry C. M., Padovani P., 1995, *PASP*, **107**, 803
 Venters T. M., Pavlidou V., Reyes L. C., 2009, *ApJ*, **703**, 1939
 Wang J.-M., Staubert R., Ho L. C., 2002, *ApJ*, **579**, 554
 Wang J. M., Ho L. C., Staubert R., 2003, *A&A*, **409**, 887
 Wang J.-M., Luo B., Ho L. C., 2004, *ApJ*, **615**, L9
 Wu Q., Cao X., 2008, *ApJ*, **687**, 156
 Wu Q., Cao X., Wang D.-X., 2011, *ApJ*, **735**, 50
 Wu Z., Jiang D., Gu M., Chen L., 2014, *A&A*, **562**, A64
 Xiao H., Ouyang Z., Zhang L., Fu L., Zhang S., Zeng X., Fan J., 2022, *ApJ*, **925**, 40
 Xiong D. R., Zhang X., 2014, *MNRAS*, **441**, 3375
 Xue R., et al., 2016, *MNRAS*, **463**, 3038
 Zdziarski A. A., Sikora M., Pjanka P., Tchekhovskoy A., 2015, *MNRAS*, **451**, 927
 Zhang L., Liu Y., Fan J., 2022, *ApJ*, **935**, 4
 Zhu S. F., Brandt W. N., Luo B., Wu J., Xue Y. Q., Yang G., 2020, *MNRAS*, **496**, 245

APPENDIX A: DERIVATION OF THE JET POWER

We list all the equations we use to calculate the jet power depending on α (viscosity parameter), j (spin of black hole) and \dot{M} (accretion rate on to the black hole) using the BZ model (Section 3.1) and the hybrid model (Section 3.2). To estimate the maximum jet power, $\alpha = 0.3$ and $j = 0.98$ are adopted. The jet power is given by equation (7) (BZ model) and equation (8) (hybrid model). The self-similar ADAFs structure is described by [Narayan & Yi \(1995\)](#). We use the black hole mass in solar units ($m = M_\bullet/M_\odot$), accretion rates in Eddington units ($\dot{m} = \dot{M}/\dot{M}_{\text{Edd}}$, \dot{M}_{Edd} is the Eddington accretion rate ($\dot{M}_{\text{Edd}} \equiv 22M_\bullet/(10^9M_\odot)$), $\dot{m} = 0.01$ is adopted ([Narayan & Yi 1995](#))) and radii in Schwarzschild units ($r = R/(2GM_\bullet/c^2)$):

$$\Omega' = 7.19 \times 10^4 c_2 m^{-1} r^{-3/2} \text{ s}^{-1}, \quad (\text{A1})$$

$$B = 6.55 \times 10^8 \alpha^{-1/2} (1 - \beta)^{1/2} c_1^{-1/2} c_3^{1/4} m^{-1/2} \dot{m}^{1/2} r^{-5/4} \text{ G}, \quad (\text{A2})$$

$$H/R \approx (2.5c_3)^{1/2}. \quad (\text{A3})$$

The Ω' is the angular velocity of the disk, B is the magnetic field strength near the black hole in terms of radius R , G is the gravitational constant, and H is the vertical half-thickness of the disk. The constants c_1 , c_2 and c_3 are defined as

$$c_1 = \frac{5 + 2\epsilon'}{3\alpha^2} g'(\alpha, \epsilon'), \quad (\text{A4})$$

$$c_2 = \left[\frac{2\epsilon'(5 + 2\epsilon')}{9\alpha^2} g'(\alpha, \epsilon') \right]^{1/2}, \quad (\text{A5})$$

$$c_3 = c_2^2/\epsilon', \quad (\text{A6})$$

$$\epsilon' \equiv \frac{1}{f} \left(\frac{5/3 - \gamma}{\gamma - 1} \right), \quad (\text{A7})$$

$$g'(\alpha, \epsilon') \equiv \left[1 + \frac{18\alpha^2}{(5 + 2\epsilon')^2} \right]^{1/2}. \quad (\text{A8})$$

where advection parameter f (assumed ≈ 1 , see Nemmen et al. (2007)), ϵ' and $g'(\alpha, \epsilon')$ are just a variable replacement. The γ is adiabatic index of the accreting fluid.

The relationship between α , β and γ is defined as follows

$$\gamma = (5\beta + 8)/3(2 + \beta), \quad (\text{A9})$$

$$\alpha \approx 0.55/(1 + \beta). \quad (\text{A10})$$

where α is viscosity parameter and β is the ratio of gas to magnetic pressure (Esin et al. 1997; Hawley et al. 1995). The angular velocity of the field seen by an outside observer at infinity in the Boyer-Lindquist frame is $\Omega = \Omega' + \omega$. Bardeen et al. (1972) gave the formula for calculating the angular velocity of the local metric as follows

$$\omega = \frac{2jM_\bullet}{j^2(R + 2M_\bullet) + R^3} \quad (\text{A11})$$

using geometrized units ($G = c = 1$). Meier (2001) estimated the field-enhancing shear caused by the Kerr metric using $g = \Omega/\Omega'$, such that the azimuthal component of the field is given by $B_\phi = gB$. The poloidal component is related to the azimuthal component following Livio et al. (1999) as $B_p \approx H/R$ $B_\phi \approx B_\phi$. In the case of an ADAFs, this yields $B_p \approx B_\phi$ because $H \sim R$. The advection parameter f is assumed $f \approx 1$ (Nemmen et al. 2007). We insert all the quantities defined above into Equations (7) and (8), and then evaluate the resulting equations at the marginally stable orbit of the accretion disk R_{ms} . Bardeen et al. (1972) defined the marginally stable orbit of the accretion disk (R_{ms}) as follows

$$R_{\text{ms}} = GM_\bullet/c^2\{3 + Z_2 - [(3 - Z_1)(3 + Z_1 + 2Z_2)]^{1/2}\}, \quad (\text{A12})$$

$$Z_1 \equiv 1 + (1 - j^2)^{1/3} \left[(1 + j)^{1/3} + (1 - j)^{1/3} \right], \quad (\text{A13})$$

$$Z_2 \equiv (3j^2 + Z_1^2)^{1/2}. \quad (\text{A14})$$

This paper has been typeset from a TeX/LaTeX file prepared by the author.